Chapter 3

THE PROBING DEPTH OF TOTAL ELECTRON-YIELD TECHNIQUES FOR X-RAY ABSORPTION SPECTROSCOPY

3.1. Introduction

Notwithstanding the fact that TEY detection is an established method for surface XAS investigations in UHV, surprisingly little attention has been devoted to the mass attenuation of the TEY signal. Only a very limited amount of experimental work has addressed the probing depth of TEY XAFS in a systematic manner, while theoretical treatments of the solid-state electron propagation/multiplication processes underlying TEY detection have never really matured beyond the state of phenomenological models [1-8]. The need for progress has recently been expressed in several experimental studies [9-13]. In particular investigations of stratified materials could benefit from better insight into the principles of TEY signal formation because *a priori* knowledge of the relevant TEY attenuation functions would pave the way to *in situ* film thickness calibrations and non-destructive depth analyses of the sample morphology and/or the electronic structure. Progress is also desirable from a technical point of view, because our fundamental insight into the relation between the X-ray absorption coefficient and the detected TEY current is still very incomplete. Despite the recent popularity of the TEY technique, uncertainties about the accuracy of the X-ray absorption information in the TEY signal have persisted for several years since several authors have reported unphysically low TEY XAFS amplitudes for a variety of sample specimens [7,11,14,15]. Origins of the amplitude reductions will be identified in chapter 4 of this thesis. Knowledge of the relevant TEY depth attenuation functions will be a prerequisite for understanding why and under what conditions the response of the TEY signal becomes non-linear.

The work described in the present chapter examines the principles which determine the depth information in the TEY signal. For the first time, Monte-Carlo simulations of electron trajectories will be applied to the calculation of the TEY signal attenuation. New experimental results for NiO-covered Ni specimens as well as literature data for the attenuation of the TEY signal in various materials will be examined by use of this method. It will be shown that experimentally determined attenuation functions can be predicted to at least semi-quantitative precision. In

contrast to earlier phenomenological methods, the calculations can be performed for any given sample specimen, taking into account both elemental composition and morphology of the sample.

3.2. Physical Principles of TEY Signal Formation

Mass absorption of X-ray photons is dominated by the photoemission of electrons which leave an atom with a core vacancy. The photoinduced core hole is unstable and decays in a cascade of inner- and outer shell transitions until the photoexcited atom attains charge neutrality [7]. Taking K-edge absorption as an example, the first decay step fills the primary K-shell vacancy with an L-shell electron. This step proceeds either by a radiationless transition (KLL Auger process) or *via* emission of a fluorescent photon. The relative probabilities of radiative and non-radiative transitions of the single core hole vary with atomic number, and have been tabulated [16]. The KLL Auger process produces a double L-shell vacancy, while the fluorescent transition simply moves the single core hole into the L-shell. The L-shell holes formed during the K-shell neutralisation undergo similar decay mechanisms as the K-holes [7,11], but the relevant transitions involve the M-shell electrons (if present) and have much reduced fluorescence probabilities [16]. The decay of the vacancies in higher shells proceeds likewise, provided that these shells are also occupied. The initial shell vacancy thus passes (and multiplies in the case of radiationless transitions) from inner shells to outer shells. Charge neutrality is finally achieved by hole-filling in the outermost atomic shell (which is, in the case of a conductor, in the valence band) by an external supply of electrons. Unfortunately, a quantitative analysis of the cascade of core transitions is made difficult by the fact that the transition rates for the decay of the multiple core holes formed in the KLL and LMM processes are only poorly understood. The physical principles underlying the formation and decay of multiple core vacancies are still the object of active research [17-21].

As a result of the various radiationless transitions, the TEY involves electrons with different initial energies. Taking K-edge absorption again as an example, most kinetic energy is carried by the KLL Auger electrons while LMM, MVV and other Auger electrons from higher shells have energies which are approximately one (LMM), two (MVV) or more (higher shells) orders of magnitude lower.

There is also a further contribution due to photoelectrons whose energy is zero at the edge step, but linearly increasing with X-ray energy. The emitted flux of these photoelectrons is therefore vanishingly small in the vicinity of the absorption edge

where insufficient energy limits the escape region for photoelectrons to a very small volume. In most experimental situations, the photoelectron contributions to the TEY become visible only at energies high above the edge, where the photoelectron energy becomes comparable to that of the Auger electron contributions [5].

In contrast, the emitted flux from the KLL Auger channel is always substantial because the energetic KLL electrons can travel a comparatively long distance to the surface before their excess kinetic energy has been thermalised. Kinetic energy and penetration range of lower-energy Auger electrons (LMM, MVV, etc.) are significantly smaller than for KLL Auger electrons so that, in bulk samples, the depth information carried by the TEY is mostly determined by the KLL emission. A more surface-sensitive contribution to the Auger yield due to LMM electrons is usually non-negligible [7]. This contribution is particularly pronounced when the thickness of the sample is of the same order as the LMM penetration range; in this case, the LMM flux can become comparable to or larger than the KLL signal.

The signal measured in the TEY experiment represents all electrons which escape from the sample surface into the ambient. An omnipresent fraction of the emitted electrons is not due to the Auger- and photoelectrons generated in the initial X-ray absorption event, but formed in inelastic scattering processes along the trajectories of the Auger- and photoelectrons in the sample specimen. The average energy of these 'true' secondary electrons (for the remainder of this work to be defined as all electrons with kinetic energies below 40 eV) is very low, with the peak of the secondary electron spectrum typically centered around a few eV and characterised by a half-width which is rarely larger than 20 eV [22-27]. Because of their low energy content, most true secondary electrons escape only from a shallow region below the surface, the thickness of which being typically less than some 100 Å (note, however, that it can significantly higher for some exceptional materials [28,29]). The rate of secondary electron production in the sample is primarily dependent on the local frequency of inelastic scattering events, so that the magnitude of the secondary electron fraction in the TEY depends critically on the number of energetic electrons (Auger- as well as photoelectrons) which pass through the near-surface region from which the secondary electrons can escape [23,25]. Accordingly, the depth information contained in the secondary yield is determined by the more energetic electrons escaping from the sample.

3.3. The Probing Depth Difference between Total Electron-Yield Detection in Vacuum and in Gas-Flow Mode. I. Experiments

3.3.1. Introduction

The principles underlying the formation of the TEY signal, as summarised in the previous section, have previously been discussed by several authors [1-8,30]. Notwithstanding this fact, all considerations of the subject have so far failed to address one important point, namely the magnitude of the secondary electron-yield contribution. The relevant views expressed in the literature are inconclusive. For example, it was argued in a widely cited study [7] that the TEY is overwhelmingly dominated by the secondary electron contribution. At the same time, it was predicted that use of gas-flow detection may enhance the surface sensitivity of TEY detection [7,31] since gas phase charge multiplication in the detector should weight the TEY signal linearly with electron kinetic energy above the gas ionisation threshold (24.6 eV for He) [32,33]. The rationale for the latter argument was that Auger electrons emerging from the sample with high energies have undergone fewer inelastic scattering events along their trajectory and hence should have originated closer to the surface than heavily scattered, lower-energy Auger electrons.

One can conjecture that the simultaneous prediction of (i) probing depth differences due to gas phase effects and (ii) dominance by the low-energy secondary electron-yield are physically difficult to justify because both phenomena are mutually exclusive. The *a priori* condition for any change of the surface sensitivity *via* gas-flow detection is a substantial energy content of the emitted flux of electrons. However, any significant excess of kinetic energy is incompatible with the view that the TEY is essentially a current of low-energy secondary electrons. In contrast, if the TEY were dominated by the low-energy secondary electrons then gas effects should be negligible, because most signal electrons would not be able to afford any charge multiplication *via* electron/ion pair formation.

Based on the interplay of KLL and LMM electron yield contributions, Erbil *et al.* derived an often cited analytical model which describes the probing depth characteristics of TEY experiments in terms of the secondary electron yield [7]. This approach was chosen because it was observed that the vacuum TEY was reduced by 90% and 60% when bias voltages of, respectively, +10.5 V and +1.5 V were placed on a Ni sample. Erbil *et al.* concluded from these data that true secondary electrons constitute more than 90% of the TEY. However, this argumentation appears questionable because it neglects the importance of wall effects in a vacuum

experiment. Energetic KLL electrons emitted from the sample induce secondary electron cascades upon colliding with the walls of the TEY equipment. As a result, secondary charges are emitted from the walls. Placing a positive bias on the sample accelerates these electrons towards the sample. Such collection of secondary electrons from the walls is increasingly efficient at larger bias voltages, as the accelerating electrical field becomes stronger. It is therefore not surprising that after increasing the positive bias to +100.5 V Erbil *et al.* measured a substantial *reversed current* through the sample. This suggests that at least some of the TEY attenuation observed at low voltages derives from cancellation of opposite currents. The secondary electron fractions derived from biasing experiments might therefore be misleading.

The possibility of a surface sensitivity difference between gas-flow and vacuum detection has not previously been addressed experimentally. Sections 3.3.2.-3.3.3. describe the results of the first comparative measurements in gas-flow and vacuum detection mode using identical samples. Unequivocal evidence for a significant probing depth difference between both detection techniques has been found. The results will also show that gas-flow detection can actually be *less* surface sensitive than vacuum experiments - contrary to earlier [7,31] predictions.

3.3.2. Experimental

Polycrystalline, diamond-polished (final grain size: 0.5 μm) Ni wafers (99.99% pure, 70 mm × 8 mm × 1 mm) covered with NiO of varying thickness were used as samples. These were prepared by controlled oxidation at 1 atm in a gas-flow furnace at 573 K and 673 K using blended air (Distillers MG, 20% O_2 / 80% N_2, 99.9% pure) which was dried from residual moisture to less than 1 ppm. The error margin for the temperature measurement was approximately 5%. Each Ni wafer was placed in the sealed furnace which was then purged for 30 min with a vigorous flow of H_2 (400 ml/min, 99.99% pure, BOC) at room temperature. Subsequently, the flow rate was reduced to approximately 50 ml/min and the furnace heated to the oxidation temperature. After 1 h of reduction in H_2, the furnace was purged with Ar (99.999%, BOC) for 30 min. Subsequently, a vigorous flow of blended air was introduced for the desired oxidation time (for oxidation times in excess of 30 min, the blended air flow-rate was reduced to about 25 ml/min). After completion of the exposure to blended air, the gas-flow was switched back to a vigorous flow of Ar to purge the furnace volume from oxidising gas components, and the furnace cooled down to room temperature.

The thickness of the oxide layers was analysed with a polarisation modulated ISA/Jovin-Ybon Uvisel® spectroscopic ellipsometer, utilising light from a Xe arc lamp in the energy range between 2 eV and 4.6 eV. A detailed account of these experiments and the data analysis is given in Appendix A. Briefly, the analysis was performed by χ^2-fitting a single, damped Lorentz oscillator model for the NiO optical constants to the dispersion of the complex dielectric constant. The optical constants of the Ni substrate were derived from measurements at a clean Ni plate, and are, within experimental error, identical to the values recommended by Palik [34]. In the analysis it was first assumed that NiO grows on Ni homogeneously as an isotropic overlayer. The result was then refined by carrying out data analyses using the Maxwell-Garnett and Brüggeman effective medium approximations [35] to account for roughness and voids in the NiO overlayer. Thus determined oxide thicknesses compare well with gravimetrically measured values reported in the literature [36-38]. The results of the spectroellipsometric analysis are summarised together with the XAFS results in table 3.1.

XAFS data were collected on beamlines 8.1 and 9.2 of the EPSRC synchrotron facility operating at 2 GeV energy and with electron currents between 100 mA and 200 mA. Rejection of beam harmonics was performed by detuning the double Si(220) monochromators to 50% of maximum reflectivity. The resulting incident X-ray flux was monitored by an ion chamber (20% absorbance at the Ni K-edge) containing a mixture of He and Ar. The details of the combined vacuum/gas-flow detector have been given in chapter 2.5. For gas-flow measurements, a constant flow of He (10 ml/min, Distillers MG, 99.99%) was maintained, while vacuum detection was enabled by a turbomolecular pump allowing evacuation of the cell to less than 5·

Table 3.1. Results of XAFS measurments and the data analysis described in Appendix A.

overlayer thickness	void fraction	NiO thickness	NiO fraction in TEY XAFS	
[Å] (± 10%)	(± 15%)	[Å] (± 25%)	He (± 0.05)	vacuum (± 0.05)
25 (native)	-	25	0	0
30	-	30	0	0.03
105	0.10	95	0	0.10
220	0.20	176	0.32	0.46
275	0.25	207	0.32	0.48
330	0.25	248	0.34	0.48
350	0.25	263	0.45	0.55
410	0.35	267	0.51	0.63
1300	0.65	455	0.70	0.73
2950	0.70	885	0.98	1

10^{-5} torr within half an hour. Measurements were carried out at $8 \cdot 10^{-6}$ torr - $2 \cdot 10^{-5}$ torr. Electrical connection to the NiO/Ni samples was made by 1 mm diameter Ni wire spotwelded to the bottom of the wafers. X-rays entered the cell within an angle of $5° \pm 2°$ relative to the sample surface plane. During all measurements, the total current from the grounded sample was collected, while an electric field was maintained by a positively biased (104 V) gold coated aluminium plate (50 mm × 12 mm × 1mm) mounted parallel at 11.2 mm distance over the sample Note that this distance is larger than the gas-phase penetration of Ni KLL Auger electrons (see section 2.7.4). A check for non-linearities of the detector geometry was made by comparing results of transmission and gas-flow experiments with a range of standard samples, including Ni (99.99 purity, 10 μm foil, see also chapter 4) and NiO (99.999% purity, ICI). Spectra measured on unoxidised, polished Ni wafers exhibited significant EXAFS amplitude reductions, for reasons which will be discussed in chapter 4.

Data were analysed according to the guidelines laid out in chapter 1. Pre-edge backgrounds were fitted with a second order polynomial function using a reference point at k = 14 $Å^{-1}$ such that the edge step was 0.9 at k = 12 $Å^{-1}$ after normalisation at the edge inflection point. Supporting analysis of the spectra was carried out with the curved wave multiple scattering code EXCURV92.

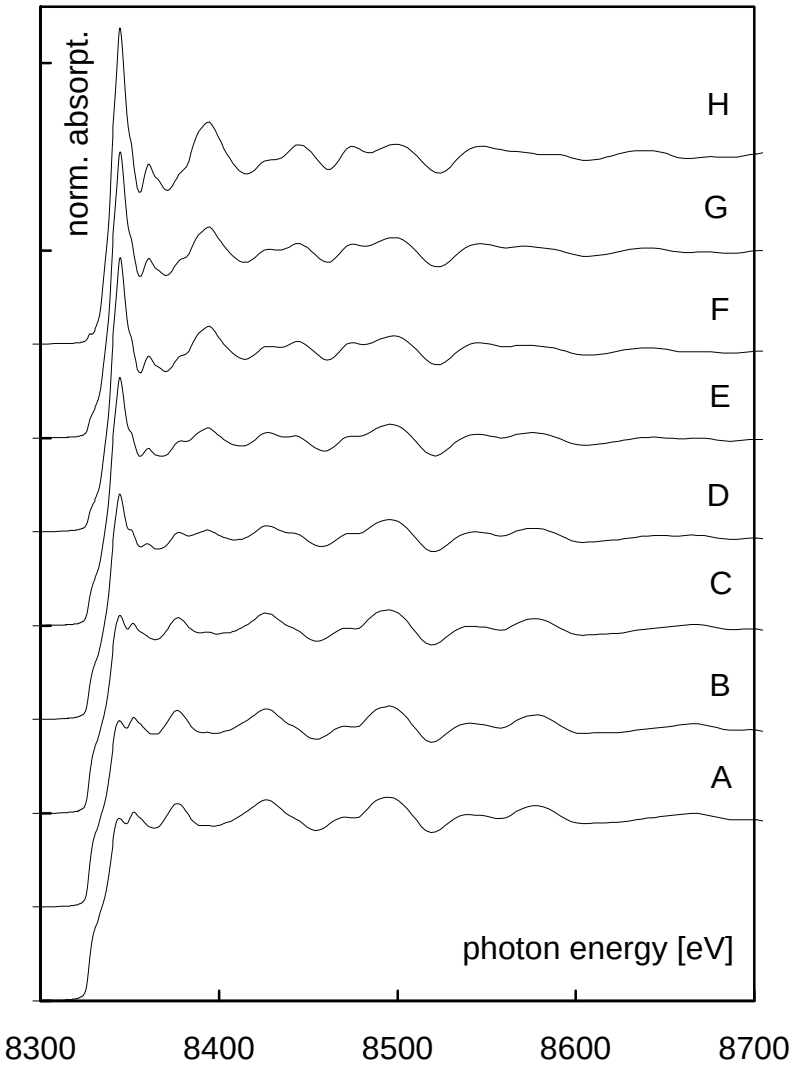

Figure 3.1 Representative pre-edge background subtracted TEY XAS data (truncated at 8700 eV for clarity). A, B, D, F: gas-flow data. C, E, G, H: vacuum data. NiO overlayer thicknesses: native oxide ≈ 25 Å (A), 95 Å (B/C), 176 Å (D/E), 455 Å (F/G), 900 Å (H).

3.3.3. Results and Discussion

Pre-edge subtracted, normalised spectra (a selection of which is shown in fig. 3.1) reveal that data collected in He contain a smaller NiO contribution than corresponding spectra collected in vacuum. This is immediately apparent (i) from the white line characteristics of the XANES regime (fig. 3.1), and (ii) from the Fourier transforms of the post-edge subtracted data (fig. 3.2). A quantitative analysis of the relative Ni and NiO contributions to the spectra was carried out by least-squares fitting linear combinations of the unweighted gas-flow TEY EXAFS from an untreated Ni plate (oxide thickness 20-30 Å) and vacuum data from a sample covered by 900 Å of NiO (for which a full analysis with EXCURV92, and comparison with a

NiO standard sample did not reveal any metallic Ni contributions). The analysis results are given in table 3.1. The quality of the fits can be judged from fig. 3.3.

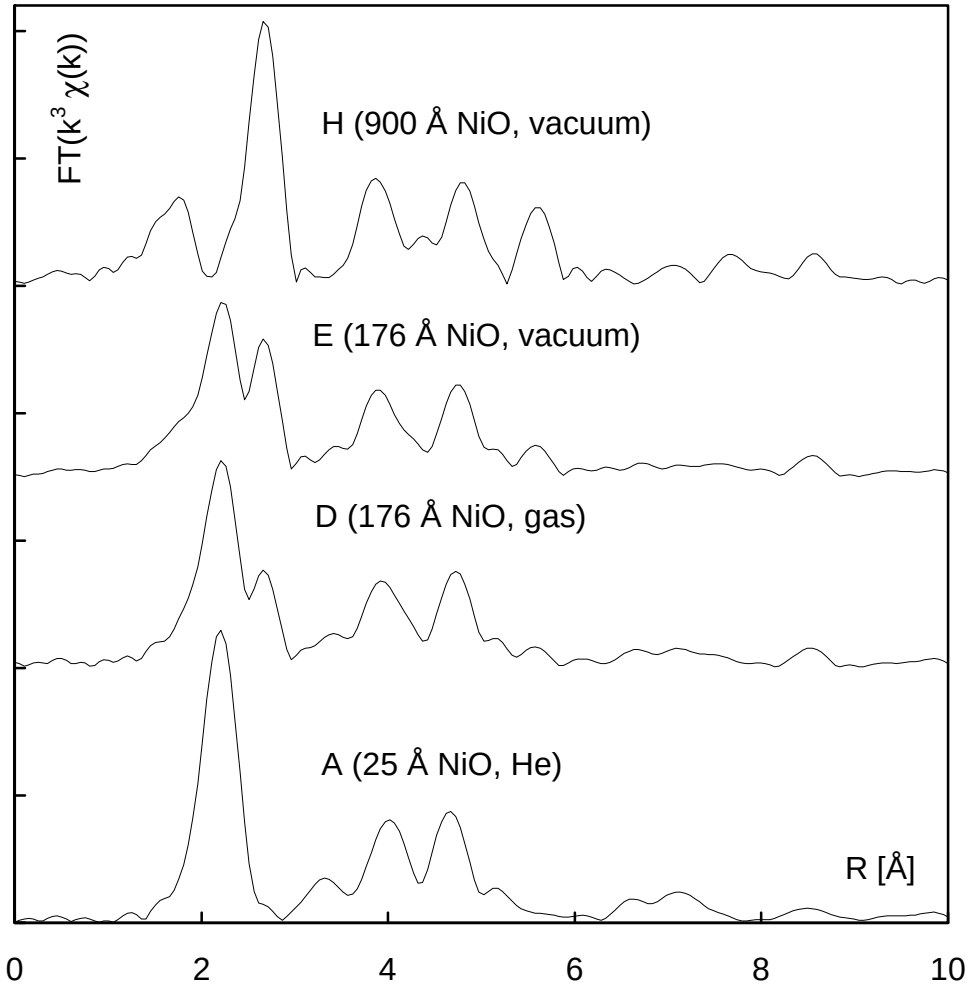

Figure 3.2. Modulus of the Fourier transforms of the k^3-weighted EXAFS derived from spectra A, D, E and H of fig. 3.1.

To explain the surface sensitivity difference between vacuum and gas-flow detection at the Ni K-edge we must consider the relative rôles of individual contributions to the TEY spectrum emitted from the sample. It was already pointed out in section 3.2 that the K-edge TEY contains not only KLL Auger electrons originating in the first step of the nonradiative K hole decay, but also Auger electrons emitted during the decay of holes in the L and M shells. The initial energy of the Auger electron contributions decreases in the order KLL > LMM > MVV (in the case of Ni from 6.5 keV to 0.85 keV and 0.06 keV respectively) [39,40]. As a consequence, KLL electrons travel substantially further through the solid than LMM and MVV electrons before their kinetic energy is dissipated, and the total flux of KLL electrons through the solid/gas interface is higher than those of LMM and MVV electrons. However, higher Auger

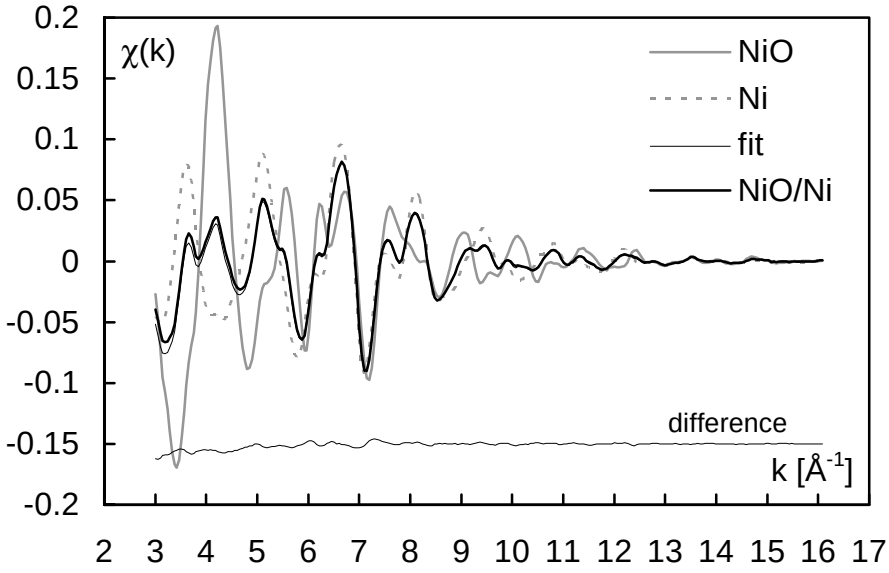

Figure 3.3 Unweighted EXAFS from spectra A (Ni, broken grey line), H (NiO, full grey line) and D (thick full line) in fig. 3.1. Thin full line: spectrum generated by linear combination of Ni (contribution: 68%) and NiO (contribution: 32%) spectra. Offset by -0.15 is the difference spectrum between D and the fit.

decay rates for L and M core holes and multiple core vacancy formation enhance the flux of LMM and MVV electrons, which, due to their low kinetic energies, can only escape from the near-surface (LMM) and very-near-surface regions (MVV). As will be discussed in more detail in section 3.4., low-energy Auger contributions are also more efficient producers of secondary electrons because the cross sections for energy losses through inelastic interactions are highest in the sub-keV energy range. Near-surface information in the TEY is therefore enhanced relative to bulk information, the latter being mainly carried by the KLL emission [7].

The probing depth characteristics of gas-flow detection must be determined largely by the energetic KLL fraction, which should dominate the signal *via* charge multiplication in the gas phase. However, amplification of the KLL fraction alone cannot be responsible for the decreased surface sensitivity relative to vacuum detection, as charge multiplication weights the KLL signal towards higher energy contributions. These latter electrons have originated *closer* to the surface than the heavily scattered fraction of lower-energy KLL electrons. The explanation for the probing depth difference between gas-flow and vacuum detection must therefore involve other contributions to the TEY. It seems most likely that the LMM Auger yield - well known to be a significant fraction of the vacuum TEY (cf. section 3.2 and ref. [7]) - plays a crucial rôle in determining the relative surface sensitivities of both detection modes. Because of the lower kinetic energy, the LMM yield is approximately one order of magnitude more surface sensitive than the KLL yield. Its

influence is expected to be less pronounced in gas-flow detection because its low energy prohibits substantial gas phase amplification. However, because the LMM contribution is also a more efficient producer of secondary electrons (cf. section 3.4), its influence should be additionally enhanced in the vacuum experiment.

Closer examination of the XAFS data reveals that secondary electrons cannot constitute the overwhelming majority of all electrons in the TEY. This is borne out by the signal amplification factors which arise due to gas-phase impact ionisation events in the He-flow measurement. When the ionisation detector is operated in the current regime then the amplification factor is a measure of the average kinetic energy of the electrons emitted from the sample. It was ensured that the gas-flow measurements were indeed performed in current mode by applying a bias of +104 V to the collector plate - well below the voltage threshold for the proportional region (where additional charge multiplication due to electron-ion avalanching occurs), but high enough to prevent electron-ion recombination (see also chapter 2 and refs. [32,33]). The influence of secondary processes occurring in the gas phase, such as molecular ion formation and the Penning effect, can, to a good approximation, be neglected. Even in unfavourable cases they are not expected to influence the amplification rate by more than about 10% - 20% [33].

A rough analysis of the amplification factor can be carried out as follows. The TEY emitted in vacuum contains a fraction x of secondary electrons and a fraction (1-x) of energetic (elastic and inelastic Auger) electrons:

$$TEY = x \cdot TEY + (1-x) \cdot TEY \,. \qquad (3.1)$$

The gas-flow TEY current is related to the vacuum TEY by the experimentally observed amplification factor A_{obs}. Only the Auger electron contributions to the TEY are amplifiable. The gas-phase amplification factor for the Auger electron contribution is given by the ratio between the average kinetic energy $\overline{E}$ of the Auger electrons and the average electron/ion pair formation loss characteristic for the detector gas. For most gases, average energy losses in a gas phase electron impact ionisation event are about 30 ± 12 eV [32,33]. The average loss in He gas, as used for the present measurements, is DE_{He} = 42.3 eV. Thus, if all kinetic energy carried by the Auger electrons is channeled into electron/ion pair production then the measured amplification factor A_{obs} is related to the fraction of secondary electrons in the TEY simply *via*

$$A_{obs} = x + (1-x) \cdot \frac{\overline{E}}{\Delta E_{He}} \,. \qquad (3.2)$$

In figure 3.4, this expression is evaluated as a function of secondary electron fraction and average Auger electron energy.

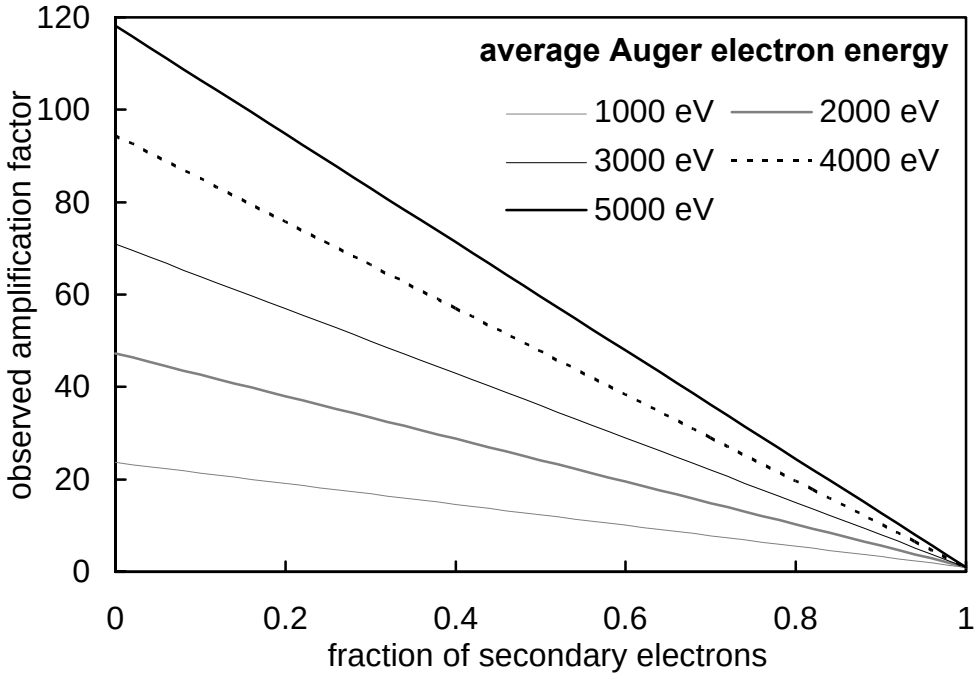

Figure 3.4.. Predicted amplification factor as a function of the secondary electron fraction in the TEY and the average Auger electron energy. The graphs were obtained assuming an electron/ion pair formation loss of 42.3 eV for each impact ionisation event in the gas phase.

Typical measured amplication factors for NiO-covered Ni wafers are 50 ± 10. The factors are higher (more than ≈ 80) for Ni wafers covered only by a native oxide film (an explanation for this observation will be given in section 3.9). Inspection of the functions plotted in figure 3.4 allows two important conclusions. Firstly, the average kinetic energy of the emitted Auger electrons must be higher than 2 keV to afford any gas amplification factor over 50. Secondly, strong gas phase amplification is incompatible with the view [7,8] that true (non-ionising) secondary electrons constitute more than 90% of the TEY: Auger electrons must be a substantial fraction of the TEY since only they have sufficient kinetic energy to afford large charge multiplication factors. The highest energy is carried by the elastic Ni KLL Auger electrons which have a kinetic energy of 6.5 keV. The average energy of all Auger electrons must be significantly lower than this. Figure 3.4. shows that a secondary electron yield fraction of more than about 70% is impossible even if the average KLL energy were 5 keV. Previous measurements in the soft and medium X-ray ranges by Henke and co-workers likewise indicated that the secondary electron yields from Al and Au surfaces do not exceed 80% (Al) and 90 % (Au) of the TEY [29]. Note also

that similarly high amplification factors as reported here were observed at the Fe K-edge, but the significance of this result was not realised at the time [41,42]. The experimental evidence therefore suggests strongly that the secondary electron contribution is actually smaller than previously believed. Supporting evidence and an explanation for this conclusion will be presented in section 3.4.

For the moment, the principal conclusion of the comparative gas-flow/vacuum study is therefore that the surface sensitivity of TEY detection in vacuum can actually be *higher* than that in gas-flow mode: this is the opposite of the commonly held view which has never really been tested before. A quantitative analysis of the probing depth difference between gas-flow and vacuum detection is not possible within the framework of models reported in the literature. The necessary calculations require the knowledge of the kinetic energy content of the TEY, and hence the calculation of approximate TEY spectra. Sections 3.5.-3.8. of this thesis will describe a model for these calculations. Using this method, a more complete analysis of the experimental results for the NiO/Ni samples will be presented in section 3.9.

3.4. Magnitude of the Secondary Electron Yield

Before proceeding to calculations of TEY attenuation functions more evidence shall be added to support the conclusion that the secondary yield does not constitute more than 90% of the TEY signal [7,8]. Small secondary yields are generally expected when the inelastic mean free path (IMFP) of the Auger electrons becomes larger than the thickness of the near-surface layer from which the secondary electrons are emitted. In this case, most Auger electrons pass through the near-surface region without experiencing any significant energy-losses. The energy dependence of electron IMFPs is theoretically well understood [43]. Several authors have derived empirical and semi-empirical calculation methods which allow the estimation of the IMFP at energies above approximately 50 eV for any given material [44-46]. The mass attenuation of the secondary electrons is more difficult to derive because our knowledge of the energy-loss cross sections which apply at very low electron energies is limited. A great deal of experimental and modeling work has nevertheless been devoted to the characterisation of the secondary electron emission in electron microscopes. Quoted figures for exponential attenuation parameters vary typically between 5 Å and 30 Å for metallic conductors [47,48], but tend to be higher for semiconductors and insulators [23,26-28,47]. Inspection of the literature suggests that 25 Å is a reasonable upper limit to the exponential attenuation length for secondary electron emission from most transition metals [47,48]. The secondary electron yield diminishes rapidly as the Auger electron IMFP surpasses this figure. A

calculation using the method of Tanuma, Penn and Powell [44] indicates that the IMFP of electrons in transitions metals exceeds this value at kinetic energies of approximately 1.6 - 2 keV. In view of these values it is not too surprising that the K-edge gas amplification factors for Fe (7.1 keV, [41]) and Ni (8.3 keV, previous section) indicate secondary electron yield contributions of less than 90% of the TEY.

Similar qualitative considerations gave rise to Salow's and Bethe's classic, semiquantitative theories for electron-beam induced secondary electron emission [49,50]. Both authors assumed that the number of secondary electrons produced along the trajectory of an energetic electron scales inversely with the energy loss rate per unit path (its 'stopping power', see below) in the sample. This simple approach reproduces most experimental features of secondary electron emission quite accurately, most notably that the rate of secondary electron emission passes, quite independent of the material, through a maximum at incident electron energies between a few 100 eV and 1.5 keV [22,23,25,48,51]. This maximum can be understood by considering the counteracting effects of kinetic energy and IMFP: at high energies, the total flux of electrons through the near-surface region is substantial, but a long IMFP prohibits the excitation of a significant secondary yield. At low energies, the cross sections for inelastic losses are large, but the number of electrons travelling through the near-surface region is small due to the strong attenuation of the internal flux of low-energy electrons. This picture has been refined in more elaborate work [23-25,51,52]. An important result of these studies is that the number of emitted secondary electrons per incident electron does, at least for conducting samples, not exceed values between 1 and 1.5 at the maximum of the secondary yield curve [23,47,48]. Dominance of the secondary yield from conductors is therefore rather exceptional even at low primary electron energies. The secondary electron emission rate per primary electron in the keV range is usually well below unity [25].

It might be argued that the previous results discussed in the last paragraph apply to electron beams being the exciting primary radiation rather than photons. The emphasis has been placed on comparisons with electron beam data simply because experimental and theoretical work on photoinduced secondary electron currents has been comparatively scarce. The few available studies indicate, however, that the characteristics of photoinduced and electron-induced secondary electron yields are quite similar [27-29]. One principal difference is that the secondary yield excited by the incident radiation is smaller for X-rays than for electrons. On the other hand, the IMFP of electrons in the keV range is usually so large that the excitation of secondary electrons by the impinging beam is small compared to the secondary yield

excited by the backscattered fraction of the incident beam [23-25,51,53,54]. Another difference between the photoexcited and electron-beam induced secondary yields derives from the fact that the core hole decay cascade after photoemission contributes Auger electrons from higher atomic shells, which, because of their lower energies, contribute more strongly to the excitation of the secondary yield. This additional contribution to the emitted yield is less significant in the case of electron beam excitation. Further modifications might apply because the angular distribution of photoexcited Auger electrons is isotropic at their point of origin, while backscattered electrons from electron beams might retain some 'memory' of their initial direction into the sample.

Finally, it should be pointed out that strong corroborating evidence for small secondary yields has recently emerged from spectroscopic studies based on carefully designed electron spectrometers [55-57]. These studies have shown that the background signal in Auger electron spectra excited by keV electron beams is dominated by backscattered primary electrons rather than by secondary electrons, a conclusion which has been confirmed by theoretical analyses of the spectral background [55,57]. Note that the opposite observation - overwhelming domination of a low-energy secondary electron 'tail' - is made when conventional spectrometers are used for the data acquisition. The secondary electron spectra obtained with standard equipment are misleading, however, because collisions of the energetic photo- and Auger electrons with the internal spectrometer walls produce an artificial secondary yield inside the analysers [55,58-61].

3.5. Total Auger Yield Model for the TEY Signal

The most important conclusion of the previous sections has been that the fraction of secondary electrons in the TEY has been overstated in the past, especially for X-ray absorption edges in the energy range above several keV. For the remainder of the present work, a very simplified view will be adopted, namely that the rôle of secondary electrons in determining the depth information carried by the TEY is only of second order importance. The depth attenuation of the TEY signal will therefore be addressed solely in terms of the Auger electron contributions. This simplification is readily justified for gas-flow TEY detection, as charge multiplication in the gas phase weights the signal strongly towards the energetic Auger electron contributions. The results of the calculations will show that the Auger yield model also provides quite accurate estimates for the TEY attenuation detected in vacuum.

A Monte-Carlo trajectory simulation model will be used to generate the Auger electron depth distribution functions (DDFs) relevant for each specimen morphology and composition. A DDF is here defined as the function $P(x)$ which gives the probability that an Auger electron originating at depth x in a sample specimen is finally emitted from the surface. This DDF approach to the interpretation of the signal attenuation function is analogous to the DDF concept previously employed for the interpretation of Auger- and X-ray photoelectron spectra [62]. It circumvents the conceptual ambiguities which have been introduced in the past by describing the TEY signal attenuation in terms of a 'probing depth', 'mean probe depth', or 'sampling depth', denoting a decay constant λ in a simple exponential attenuation law of the form $P(x) \mu exp(-x/l)$ [9,10,41,63-65].

Use of the exponential law defines the 'probing depth' λ implicitly as the thickness of the near-surface region from which the fraction 1 - 1/e (63.2%) of the emitted signal originates. The *a priori* choice of an exponential attenuation law is physically difficult to justify, however, as the TEY signal is a superposition of contributions from individual Auger decay channels with different attenuation characteristics. Much less restrictive is the description of the TEY attenuation in terms of an *information depth*, which is defined, independent of the relevant experimental- and material parameters, as the distance from the surface from which a specified fraction of the signal originates [62,66]. If the TEY signal attenuation were to obey the exponential attenuation law, then the 'probing depth' λ would still be equivalent to an information depth defined as the thickness of the near-surface layer from which the fraction 1 - 1/e of the TEY signal originated. However, any other mathematical form for the attenuation function (such as the superposition of Auger electron DDFs to be described below) can also be accommodated within the definition of the information depth. Throughout the remainder of this study, the term 'probing depth' will therefore be taken to denote only an information depth defined by the 1 - 1/e (63.2%) boundary.

Assuming that the X-ray absorption length is much larger than the mean escape depth of the Auger electrons, and that X-ray absorption and Auger electron emission are both isotropic in angle, the emitted flux $I_k(x)$ of Auger electrons originating in a radiationless decay process (subsequently denoted as KLL, LMM, etc. in place of the subscript k) can be expressed as a function of the depth distribution function $P_k(x)$ according to:

$$I_k(x) \propto I_0 \cdot P_k(x) \cdot n_k \qquad (3.3)$$

where I_0 is the incident flux of X-ray photons and n_k arises because of the differences in the radiationless decay probabilities a_k (tabulated in [16]) for different core holes. The relevant expressions for n_k in a K-edge X-ray absorption have already been derived elsewhere [7]. Briefly, each K-edge absorption event generates on average

$$n_{KLL} = a_{KLL} \qquad (3.4)$$

KLL electrons [16] and an equal number of double L-shell holes. Every radiative decay event produces an additional single L-shell vacancy. Assuming that all L-shell vacancies decay non-radiatively with the same probability a_{LMM}, the total number of LMM electrons is given by [7]

$$n_{LMM} = 2 \cdot a_{KLL} \cdot a_{LMM} + \frac{K_a}{K_a + K_b} \cdot w_K \cdot a_{LMM} \qquad (3.5)$$

where w_K is the probability for radiative decay of the K-shell core hole [16] and K_a/K_b the emission rate ratio for K_α- and K_β-fluorescence [67]. The simplification that the value of a_{LMM} is the same for each L-vacancy, irrespective of the presence of a singly or doubly ionised L-shell, is a good approximation for most elements, because L-shell Auger yields are close to unity throughout large sections of the periodic system [16] and multiple core vacancies favour the decay *via* the Auger channel [17,20,21,68-70]. The approximation is likely to break down for the elements of the second period, where the L-shell is part of the valence region, and at very high atomic numbers, for which the L-shell Auger yield deviates significantly from unity. Further corrections to the LMM flux are expected as a result of photo- and electron-impact ionisation of the L-shell by self-absorbed fluorescence and KLL electrons.

For evaluations of the TEY signal from thin film samples, integration of function (3.3) and summation over all available Auger decay channels *k* according to

$$i(d) \propto \sum_k \int_0^d I_k(x) \cdot dx \qquad (3.6)$$

gives the total Auger yield *i(d)* expected from a film of thickness d. However, for almost all results reported in the literature the incident X-ray flux I_0 is unknown so that only the attenuation of a normalised signal $i_n(d)$

$$i_n(d) \propto \sum_k \int_0^d I_k(x) \cdot dx \Big/ \sum_k \int_0^\infty I_k(x) \cdot dx \qquad (3.7)$$

can be evaluated.

What has previously been little appreciated is the fact that evaluations of the TEY signal attenuation data for samples covered by overlayers of varying thickness require a fundamentally different approach. In this case, one is interested in the total emitted current $I_k(t)$ as a function of overlayer thickness t. Determining $I_k(t)$ is equivalent to integrating the DDFs $P_k(x,t)$ which characterise the Auger electron emission from the sample of thickness d under the attenuating layer:

$$I_k(t) \propto I_0 \cdot n_k \cdot \int_0^d P_k(x,t) \cdot dx\,. \qquad (3.8)$$

The TEY $i(t)$ emitted from the sample as a function of overlayer thickness t is then given by

$$i(t) \propto \sum_k I_k(t)\,. \qquad (3.9)$$

3.6. Comparison with the Secondary Electron-Yield Model of Erbil *et al.*

The relation between the often cited TEY signal attenuation model of Erbil *et al.* and the pure Auger yield approach outlined above is easily elucidated. The following reinterpretation will show that the basis of the previous model is essentially equivalent to the present Auger yield approach, except for a different mathematical form for the Auger electron DDF and the inclusion of a constant amplification factor which takes account of secondary electron production.

Erbil *et al.* assumed that the TEY current is overwhelmingly dominated by the flux of the secondary electrons and derived a simple analytical model to estimate the probing depth [7]. Krol *et al.* have presented a more generalised secondary yield model [8] which essentially confirmed these conclusions. The model in ref. [7] attempts to reproduce the secondary electron formation process by making five key assumptions: (i) secondary electrons dominate the TEY, (ii) every Auger electron produces an isotropic distribution of N secondary electrons throughout the volume of the sphere defined by the Auger electron penetration range R_p (defined as the maximum

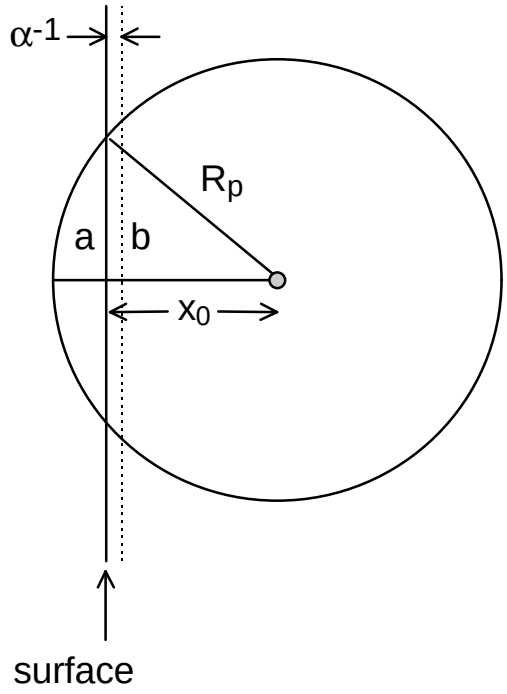

Figure 3.6. Geometrical relationships underlying the secondary yield model for the TEY developed by Erbil *et al.*

straight-line distance to its origin that the Auger electron can reach, cf. fig. 3.6), (iii) the number N of secondary electrons formed in the penetration sphere is given by the ratio E_A/ε between the initial Auger electron energy E_A and the average pair formation energy loss ε (the average energy-loss experienced per generated secondary electron), (iv) the velocity distribution of the secondary electrons is isotropic, and (v) the depth attenuation of the secondary electrons created a distance x away from the surface follows an exponential attenuation law with a decay parameter α^{-1} which is assumed to be much shorter than the Auger electron penetration range R_p. As shown in the original work, these assumptions lead to the following expression for the TEY attenuation in terms of a sample current $I(x_0)$ (wherein x_0 denotes the point of origin of the Auger electron with respect to the sample surface) [7]:

$$I(x_0) \approx \frac{3}{8} \cdot \frac{E_A}{e \cdot a \cdot R_p} \cdot \left[1 - \left(\frac{x_0}{R_p} \right)^2 + 2 \cdot \frac{x_0}{R_p} \cdot \frac{1}{a \cdot R_p} - \frac{2}{(a \cdot R_p)^2} \right]. \quad (3.10)$$

Closer examination of this expression reveals that the decisive term in the square brackets is the function $1 - (x_0 / R_p)^2$. Since $a^{-1} << R_p$ this function can also be interpreted as a normalised DDF for each Auger decay channel. This becomes clearer with a simple geometrical argument. Figure 3.6 illustrates the geometrical

relationships underlying the model of Erbil *et al.* It is seen that the sample surface cuts at the distance x_0 through the sphere defined by the Auger electron penetration range R_p, defining the surface area $S(x_0) = \pi \cdot a^2 = \pi \cdot (R_p^2 - x_0^2)$ which is proportional to the escape probability for the Auger electron because the model assumes that the probability of finding the outgoing Auger electron wave remains constant throughout the penetration sphere. The maximum escape probability exists for electrons emitted at the sample surface, where x_0 = 0, and hence $S(x_0 = 0) = \pi \cdot R_p^2$. The ratio

$$P_E(x_0) = \frac{S(x_0)}{S(x_0 = 0)} = 1 - \left(\frac{x_0}{R_p} \right)^2 \qquad (3.11)$$

gives the escape probability for the Auger electrons as a function of origination depth x_0 normalised to the escape probability at the surface, in other words: a normalised Auger electron DDF $P_E(x_0)$. In line with this, the function

$$I(x_0) \approx \frac{3}{8} \cdot \frac{E_A}{e \cdot a \cdot R_p} \cdot \left[1 - \left(\frac{x_0}{R_p} \right)^2 \right] = A \cdot P_E(x_0) \qquad (3.12)$$

yields almost the same results as Erbil *et al.'s* original attenuation function (3.10). The physically rather unrealistic form of the Auger electron attenuation DDF in equation (3.11) is responsible for the abrupt cut-off of the calculated TEY signal attenuation function close to the maximum penetration range.

Equation (3.12) shows also that the result of Erbil *et al.* essentially includes the influence of the secondary electron-yield as a constant charge multiplication factor A. In the limit of x_0 = 0 a convenient interpretation of this amplification factor can be derived if one assumes that all secondary electrons produced in a layer of thickness a^{-1} subsequently escape from this region. Figure 3.6 illustrates that the near-surface layer defined by a^{-1} represents geometrically a segment of two bases of the penetration sphere. Using a and b as the radii of the bases, the segment volume is calculated as $1/6\,\pi a^{-1}(3a^2 + 3b^2 + a^{-2})$. Because of the assumed isotropic distribution of secondary electrons, the ratio between the segment volume and the total volume of the penetration sphere ($4\pi R_p^3/3$) defines the fraction of secondary electrons originating within the near-surface layer. The total number of secondaries produced within the penetration sphere is given as E_A/e. Setting a and b equal to R_p

(a good approximation since $a^{-1} << R_p$) and accounting for the fact that only half of the secondary electrons will travel towards the sample surface (the other half moves into the sample and is reabsorbed) yields exactly the amplification factor A defined in equation (3.12):

$$A \approx \frac{1}{2} \cdot \frac{E_A}{e} \cdot \frac{a^{-1} \cdot (6 \cdot R_p^2 + a^{-2})}{8 \cdot R_p^3} \approx \frac{3}{8} \cdot \frac{E_A}{e \cdot a \cdot R_p}, \quad (3.13)$$

(where the second approximation can be made again because $a^{-1} << R_p$). This derivation explains the insensitivity of the model of Erbil *et al.* to the actual values of the parameters e and a^{-1}, since both parameters influence only through the constant A. The topology of the calculated TEY attenuation function is therefore almost solely defined by the normalised Auger electron DDF given by equation (3.11). It is therefore not too surprising that Erbil *et al.* obtained reasonable fits to several sets of experimental data by assuming an average pair formation energy loss of 8 eV and a secondary electron escape depth of 5 Å, despite the fact that comparison with literature data suggests that both values severely underestimate the true figures [48]. In particular the low escape depth for the secondary electrons, if real, would be incompatible with any appreciable rate of KLL induced secondary emission since the inelastic mean free path (IMFP) of almost all Auger electrons would be greater than the quoted value of 5 Å for the secondary electron escape depth. The resulting low frequency of inelastic interactions in the near surface region would lead to a very small secondary yield. A shortcoming of the model is that it breaks down for low energies where the Auger electron penetration range is so short that the condition $a^{-1} << R_p$ is no longer fulfilled. For example, typical secondary electron escape depths, a^{-1}, for first-row transitions metals, are approximately 25 Å, of the same order of magnitude as LMM penetration range in these materials. For other materials (e.g. CsI [28]) the secondary electron escape depth is so long that Erbil *et al.'s* model would yield sensible results only at very high electron energies.

3.7. Monte-Carlo Algorithm for Auger Electron Trajectory Simulations

Important for Monte-Carlo calculations of electron penetration are accurate cross sections for the simulation of the elastic electron-atom scattering events [51,71,72]. It has long been recognised that the importance of relativistic effects at energies below 10 keV requires exact solutions of the Pauli-Dirac equation for the elastic scattering problem [71,73-77]. Tabulations of exact relativistic cross sections (often referred to as 'Mott' cross sections) for most elements have been published, e.g. in [78-81], but

Monte-Carlo simulations based on tables are time-consuming due to the extra computation time required for interpolating between the tabulated values. To avoid these complications, simple analytical expressions have recently been derived which approximate the relativistic cross sections in a closed mathematical form [82-84]. Such semi-empirical cross sections enable fast simulations and make calculations tractable on small computers. The present work employs an implementation of Browning's algorithm [82,85,86]. This algorithm has initially been developed for fast calculations of electron penetration information for specimens examined by electron microscopies. An excellent description of the principles underlying this algorithm was recently given by Reimer and Senkel [73]. Briefly, the calculations are based on an analytical expression which has been derived from smooth empirical fits to the exact elastic scattering cross sections (s_{el}) calculated by Czyzewski et al. [78]. The resulting universal equation for the total elastic scattering cross section s_{el} depends only on the atomic number Z and the electron energy E (in eV):

$$s_{el} = \frac{3 \cdot 10^{-18} \cdot Z^{1.7}}{E + 0.005 \cdot Z^{1.7} \cdot E^{0.5} + 0.0007 \cdot Z^2 / E^{0.5}} \text{ [cm}^2\text{]}. \quad (3.14)$$

The elastic mean free path l_{el} in the sample is given by

$$l_{el}^{-1} = \frac{r}{M} \cdot N_A \cdot s_{el} \text{ [cm}^{-1}\text{]} \quad (3.15)$$

where r is the material density (in g/cm^3) and M the atomic weight (in g/mol). The scattering angles are calculated using a modified Rutherford prescription for the generation of polar and azimuthal scattering angles [73,82]. While individual trajectories calculated with this method lack some of the accuracy which could be achieved by using more exact cross sections, averaging over a sufficiently large ensemble provides meaningful electron penetration information since most quantum features of the exact cross sections are also averaged out in the multiple scattering process that leads to the electron ejection from the sample surface. It has been shown that electron backscattering factors as well as transmission information calculated with the Browning algorithm agree well with results obtained by more elaborate simulations and experimental data [82]. The present implementation of the algorithm has successfully been tested to reproduce previous results.

The simulations take inelastic scattering and energy losses of the travelling electrons into account *via* a continuous slowing-down (CSD) expression for the stopping power (defined as the energy loss dE per travelled path dl) of the material. For the

results reported here, the semi-empirically modified Bethe law of Joy and Luo [87] was used:

$$\left(\frac{dE}{dl}\right) = -785 \cdot \frac{r \cdot Z}{M \cdot E} \cdot \ln\left(\frac{1.166 \cdot (E + t \cdot J)}{J}\right) \text{ [eV/Å]} \quad (3.16)$$

where J is the mean ionisation potential (in eV) of the material. The dimensionless constant t was fixed for all calculations at 0.85, neglecting a small material dependence [87]. It is easily verified that the error thus introduced into the calculated stopping powers never exceeds a few percent, almost certainly remaining within the error margins introduced by other approximations made in the derivation of the Browning algorithm [82]. The mean ionisation potential was calculated according to [88]:

$$J = 9.76 \cdot Z + 58.5 \cdot Z^{-0.19} \text{ [eV]} \quad \text{for Z > 12} \quad (3.17)$$

and for elements with Z < 13 the values recommended in [89] were used. The merits of the stopping power expression of Joy and Luo are (i) that it has a simple analytical form enabling fast calculations and (ii) that its accuracy at low electron energies appears to be greater than for other semi-empirical CSD expressions.

The algorithm considered an electron as non-contributing to the TEY when it had never crossed the interface and its energy had dropped below 40 eV. The energy cut-off was necessary because of the inaccuracy of the CSD approximation at energies below 50 eV. If the initial Auger electron energy is sufficiently high (above approximately 1 keV) then the cut-off has no pronounced influence on the calculated results since the residual electron range (on the order of one IMFP) is small compared to the range covered by the electron before its energy has dropped below the 40 eV threshold.

Some caution in applying the CSD approximation is nevertheless advisable since energy-loss rates in some materials might deviate significantly from the predictions of the simple CSD theory. Stopping power calculations at low electron energies should ideally be based on accurate cross sections for the individual energy loss channels characterising each material [71,90]. The present algorithm has nevertheless been shown to achieve good agreement with experimental transmission data for electron energies as low as 1 keV. Towards even lower energies the accuracy of the predicted results is likely to become worse, but the error is unlikely to become so large as to impair semiquantitative estimates of TEY attenuation functions. Future theoretical and experimental work will have to clarify the limits of the present

approach, particularly for absorption edges in the sub-keV energy range. As a first step in this direction, the CSD expressions of Love *et al.* as well as Rao-Sahib and Wittry [91,92] have been tested for comparison. Significant deviations between simulation results based on the different CSD approximations were only found for initial electron energies below approximately 0.8 keV.

Several extensions to Browning's original algorithm were necessary for calculations involving compounds and heterogeneous samples. For compounds, additivity of the elemental scattering and stopping power properties was assumed ('Bragg's rule' [93-96]). The resulting expressions for stopping power [94-96], mean ionisation energy (J_c) [94,97], and the elastic mean free path (λ_{el}) [96,98] of the compound then become

$$\left(\frac{dE}{dl}\right)_c = -785 \cdot \frac{r_c}{M_c \cdot E} \cdot \ln\left(\frac{1.166 \cdot (E + t \cdot J_c)}{J_c}\right) \cdot \sum_{i=atoms}^{n} Z_i \quad \text{[eV/Å]} \qquad (3.18)$$

$$\ln J_c = \frac{1}{Z_c} \cdot \sum_{i=atoms}^{n} Z_i \cdot \ln J_i \quad \text{[eV]} \qquad (3.19)$$

$$l_{el}^{-1} = \frac{r_c}{M_c} \cdot N_A \cdot \sum_{i=atoms}^{n} s_{el,i} \quad \text{[cm-1]} \qquad (3.20)$$

where r_c, M_c, and J_c are the density (in g/cm3), molecular weight (in g/mol) and mean ionisation potential (in eV) of the compound. Z_c is the total number of electrons per chemical formula unit, whereas Z_i, J_i and $s_{el,i}$ represent the atomic numbers, mean ionization potentials and elastic scattering cross sections (in cm2) of the individual atomic species denoted by the subscript i. N_A is Avogadro's number and n the total number of atoms in a formula unit of the compound. The calculation of scattering angles with the modified Rutherford prescription requires further that an atom species is identified with each scattering event. In the present implementation, this was done by evaluating the partial elastic scattering cross sections $\bar{s}_{el,k}$ of each atom (denoted k) in the formula unit, as defined by:

$$\bar{s}_{el,k} = s_k \Big/ \sum_{i=atoms}^{n} s_{el,i} \,. \qquad (3.21)$$

Each partial scattering cross section defines a unique interval between 0 and 1, *i.e.*, the intervals

$$(0,\ \bar{s}_{el,1}),\ (\bar{s}_{el,1}, \bar{s}_{el,1}+\bar{s}_{el,2}),\ (\bar{s}_{el,1}+\bar{s}_{el,2}, \bar{s}_{el,1}+\bar{s}_{el,2}+\bar{s}_{el,3}),\ldots,$$
$$(\bar{s}_{el,1}+\bar{s}_{el,2}+\ldots+\bar{s}_{el,n-1},1),$$

so that the scattering atom *i* can be determined by choosing a random number $RND \in (0,1)$ which identifies the scattering atom by the interval which contains *RND*. In the case of a binary compound of stoichiometry A_aB_b this is equivalent to choosing *RND* such that atom A is the scatterer when

$$RND < \frac{a \cdot s_{el,A}}{a \cdot s_{el,A} + b \cdot s_{el,B}} \qquad (3.22)$$

and atom B otherwise.

For each trajectory the initial direction of electron propagation was chosen randomly. The geometrical transformations along the trajectory were calculated as described in Appendix A of reference [99]. Interior and exterior of the sample were treated as semi-infinite media. Every electron trajectory crossing the interface between the half-spaces was counted as a signal electron. The kinetic energy of all signal electrons was stored in memory and assembled into a 20-grid electron spectrum after completion of the simulation. For a trajectory crossing an interface *within* the sample the direction of electron motion was maintained, but the trajectory was corrected for the stopping power change at the interface. All effects of electron reflection/refraction at grazing electron incidence with respect to the interface and straggling of the electron energy were neglected. The calculations were carried out on personal computers based on 80386, 80486, and Pentium® CPUs, using the built-in random number generators. All simulation results were obtained with a minimum number of 5000 trajectories per datapoint. Depending on the initial electron energy, computation times on a 33 MHz 80486DX system varied between a few minutes and a few hours for a total of 100,000 trajectories. Note that considerably smaller numbers of simulated trajectories are in practice sufficient to obtain useful results. A user-friendly implementation of the Monte-Carlo algorithms, to be based on the graphical Windows® interface, is in preparation. Executable copies will be made available upon contacting the author.

For the calculation of the TEY attenuation in a gas-flow detector it was assumed that all residual energy of the emitted electrons is channeled into impact ionisation of gas phase particles. The total number of gas phase charges per emitted electron was

obtained by dividing the residual kinetic energy of each emitted electron by the average energy for pair formation in He (42 eV [32,33]). The resulting difference in the calculated signal is illustrated in figures 3.7. and 3.8. Figure 3.7. compares the calculated Cu KLL emission spectrum, as it would be detected in a vacuum measurement, to the corresponding Cu KLL spectrum claculated for a gas-flow environment. Both spectra have been normalised to the maximum intensity at the highest energy. It is clearly seen that charge amplification in the gas phase weights the signal towards the high-energy contributions. As the high-energy contributions have undergone a smaller number of inelastic scattering events in the sample, they have travelled a shorter average distance to the sample surface. In line with this, the gas-flow KLL spectrum exhibits a higher surface sensitivity as the spectrum obtained in vacuum. This is illustrated in fig. 3.8. which contains the normalised DDFs corresponding to the calculated spectra in fig. 3.7. Remember, however, that the overall surface sensitivity of TEY detection in vacuum does also depend on the LMM contributions (cf. section 3.3) and, under certain experimental circumstances, on secondary electron production (cf. section 3.9).

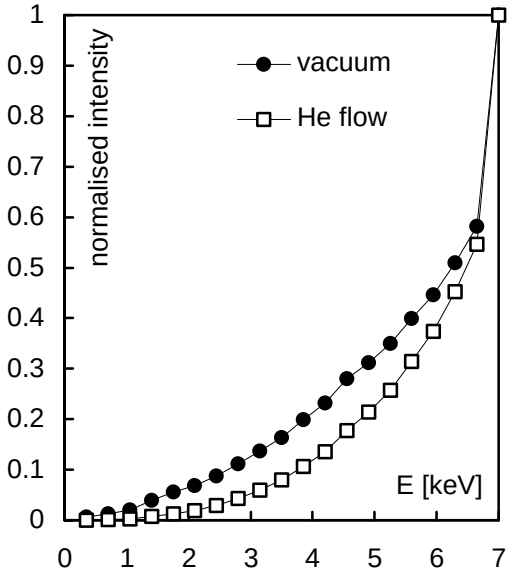

Figure 3.7. (left) Comparison of the calculated Cu KLL emission spectrum from metallic Cu for detection in vacuum and in He. The spectra represent the evaluation of 150,000 trajectories.

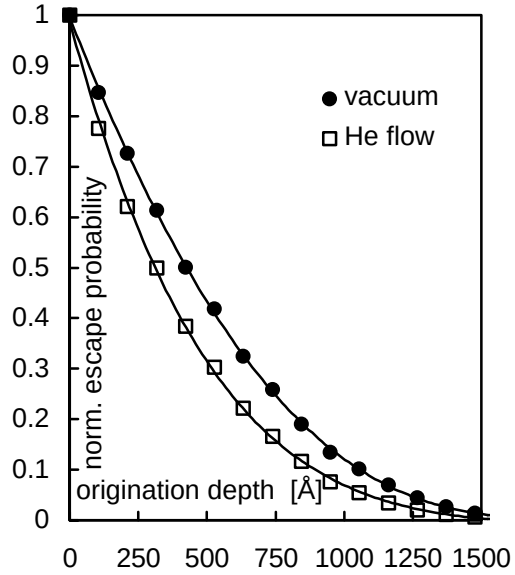

Figure 3.8. (right) Comparison of the vacuum- and He gas-flow Cu KLL DDFs corresponding to the spectra given in fig. 3.7. Each datapoint represents the evaluation of 10,000 trajectories.

3.8. Analysis of Experimental Data Using the Auger-Yield Model

3.8.1. Previously Reported Results

The choice of TEY attenuation data for comparison with theoretical calculations is still very limited. For gas-flow detection, experimental probing depth results were reported for the first time by Bouldin *et al.* [31], who estimated very rough values between 700 Å and 1000 Å for the probing depth in amorphous GaAs (Ga K-edge, 10.37 keV) and in metallic Fe (Fe K-edge, 7.11 keV). Tourillon *et al.* claimed sampling depths of substantially less than 100 Å for Au layers on Ni (Au L_3-edge, 11.92 keV) [100]. In a later study by the same group of authors these low figures were not confirmed. Instead, exponential attenuation functions were fitted to attenuation data for Cu, W/WO_3 mixtures, Ni/Ti and Co/Ti alloys [101], all exhibiting decay parameters in the order of several 100 Å. Elam *et al.* found good agreement with experimental attenuation data for Al overlayers on Fe by fitting the attenuation characteristics of Al at the Fe K-edge (7.11 keV) with an exponential law using a decay coefficient of 1639 Å [41]. To the author's knowledge, other studies of the information depth of gas-flow TEY detection have not been described in the literature.

The earliest experimental investigation of the depth attenuation of vacuum TEY detection was carried out for Cu overlayers on a Ni(111) crystal [102]. Jones, Woodruff and co-workers [63] evaluated the probing depth characteristics of Al and Al_2O_3 at the Al K-edge (E = 1.56 keV). They applied an exponential attenuation law to their data and found best agreement with experiment by using an attenuation parameter of 65 Å for Al and 130 Å for Al_2O_3. Very recent experiments by Abbate *et al.* [9], as well as by Vogel and Sacchi [10], addressed the probing depth characteristics for soft X-rays in vacuum. Exponential attenuation laws were used to obtain decay constants of 25 Å (in Tb, E = 0.85 keV) [9], 19 Å (in Ta_2O_5, E = 0.53 keV) [9], and 11 Å (in Dy, E = 0.85 keV) [10] were found. Very recently, a study by Ebel *et al.* [65] reported results for the depth attenuation of the TEY signal in Fe, Cu and GaAs based materials, but experimental details given in this brief report were scarce, making it difficult to assess the quality of the data. Nevertheless, their results seem to be in good agreement with previous studies.

3.8.2. TEY Signal Attenuation in Metals

Vacuum TEY data for the Cu K-edge signal attenuation in Cu metal have been reported for films of varying thickness supported on Fe- [65] and Ni-substrates [102].

The DDFs which are relevant for the analysis of this system are given in figure 3.9. Included are the Cu KLL (7000 eV) as well as the Cu LMM (920 eV) electron attenuation functions for Fe, Ni and Cu. The calculated results reveal clearly that the scattering and slowing-down properties of the three materials are almost identical. This conclusion is in line with previous calculations of inelastic (e.g. in [103]) and elastic mean free paths (e.g. in [98]) which likewise indicated that the scattering properties of the three transition metals are very similar. The close agreement between the electron attenuation properties arises from similarities in atomic numbers, mass densities, atomic weights and valence shell structures. As a result, the differences between the electron scattering characteristics of the metals are small enough to justify an interpretation of the Cu TEY data simply in terms of the attenuation characteristics of pure Cu metal, ignoring small deviations due to the different backscattering properties of the underlying substrates.

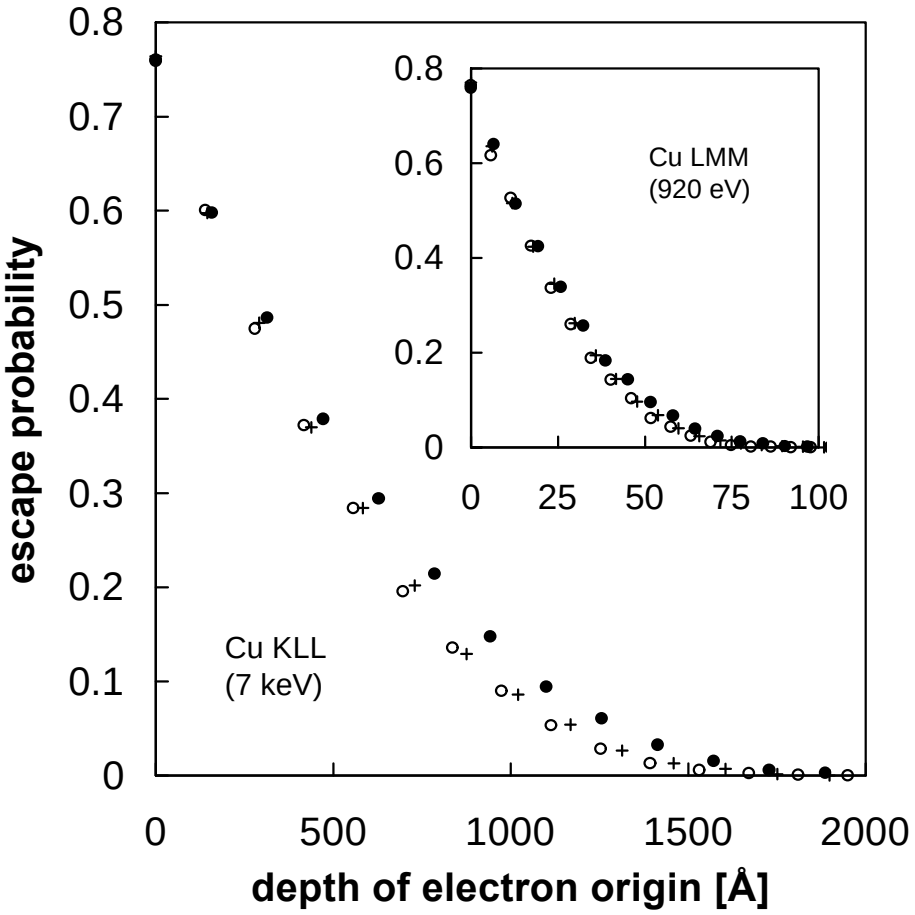

Figure 3.9. Calculated Auger electron DDFs $P_{LMM}(R)$ and $P_{KLL}(R)$ for Cu Auger electrons penetrating Fe (filled circles), Ni (open circles) and Cu (small crosses). The main graph shows the results for Cu KLL electrons and the inset for Cu LMM electrons. Each datapoint represents the evaluation of 10,000 trajectories.

Figure 3.10. illustrates that these differences are in fact also negligible when the medium-Z supports Fe, Ni and Cu are replaced by a relatively low-Z support, such as the quartz (SiO_2) wafers chosen in a gas-flow Cu K-edge study by Girardeau *et al.* [101]. The simulations predict a slightly different TEY signal with respect to that observed for bulk Cu, but only in the case of very thin Cu films. The observed lowering of TEY signal arises from the reduced backscattering ability of low-Z elements. The predicted effect (fig. 3.10) is so small, however, that it is unlikely to become apparent in experimental results.

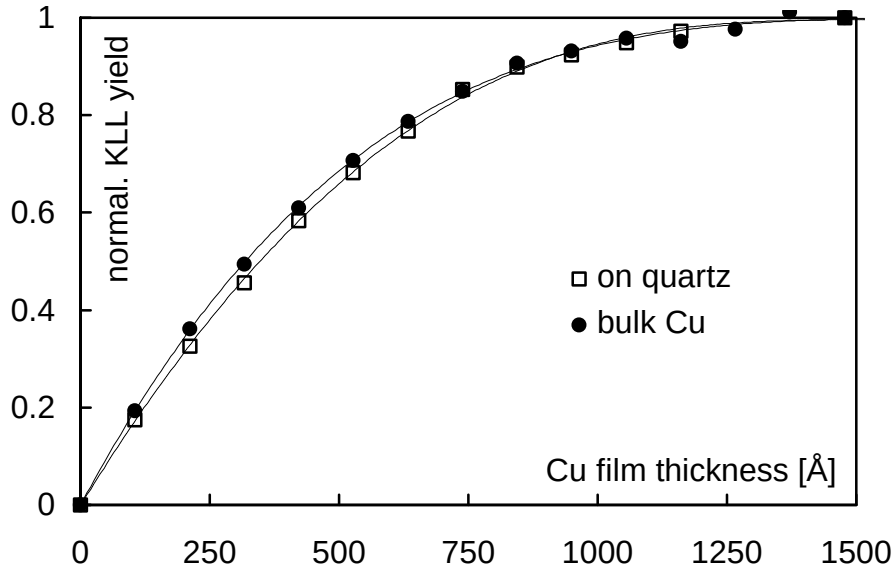

Figure 3.10. Comparison of the calculated Cu KLL signal as a function of Cu film thickness for bulk Cu (filled circles) and films supported on a quartz substrate (open squares).

The calculated results for the dependence of the Cu K-edge TEY on Cu film thickness are compared to experimental data in figs. 3.11. (vacuum) and 3.12. (gas-flow). The calculations for the vacuum data were carried out using both the Cu KLL (E_0 = 7000 eV) and Cu LMM (E_0 = 920 eV) emission. Since the photon flux I_0 was not reported for the experimental data [65,102], only a normalised edge step current according to equation (3.7) was evaluated. The gas-flow data were simulated including only the energetic KLL channel. The agreement between calculated and experimental data is in all cases very satisfactory, especially for the gas-flow data. Agreement between calculation and experiment is at least semiquantitative. An approximate error of 20% - 40% with respect to the film thicknesses would be made if the present Monte-Carlo simulation model would be applied to predict relative experimental signal intensities. Deviations from experimental vacuum data are mostly seen for higher Cu film thicknesses were the calculations generally

overestimate the attenuation power of the Cu films. This result is not unexpected because the calculations have neglected several factors which increase the experimental signal of TEY contributions from deeper sample regions. These include straggling, oxidation, roughness and porosity of the Cu films as well as TEY contributions excited by fluorescent photons and systematic errors in the film thickness calibrations. Note that the TEY currents reported by in the study of Ebel *et al.* [65] are lower than those of Martens *et al.* [102] at almost all Cu film thicknesses (fig. 3.11.). The KLL induced secondary electron yield should also become more pronounced with increasing film thickness because of the larger numbers of heavily scattered KLL Auger electrons which arrive in the near-surface region. These KLL electrons have relatively low energies and therefore shorter IMFPs, resulting in an increased probability for the excitation of secondary electrons. It is interesting to note that the results of the calculations agree much better with the experimental vacuum data for film thicknesses below 200 Å where the influence of straggling and KLL induced secondary electrons must be weak. Corrections to the calculated attenuation function in this region are mainly expected to result from LMM induced secondary electron yield and uncertainties in the CSD approximation at low energies.

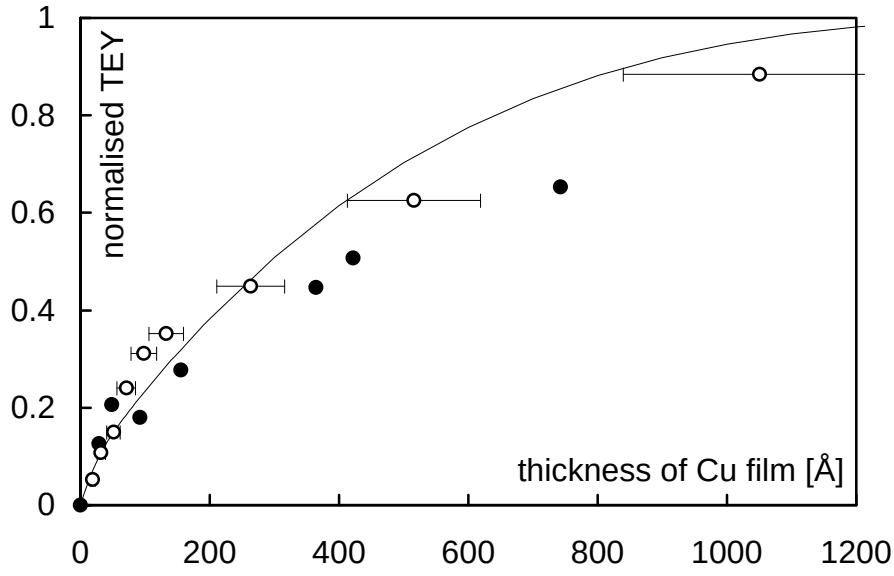

Figure 3.11. Vacuum signal attenuation function for the Cu K-edge TEY of metallic Cu calculated from the Cu KLL/LMM DDFs given in fig. 3.9 and compared to experimental signal attenuation results for Cu films deposited on Ni(100) (open circles, [102]) and Fe (filled circles, [65]). No error bars were reported for the data in [65]. The full line was derived using 3rd order polynomial fits to the Cu KLL and LMM DDFs presented in fig. 3.9.

An analysis was also made of the attenuation of the Fe K-edge signal from Fe metal as a function of Cu metal overlayer thickness. Some of the calculated Fe KLL DDFs

($P(x,t)$) for varying Cu film thicknesses (t) are given in fig. 3.13. Fig. 3.14. compares the resulting attenuation function $i(t)$ to experimental data of Ebel *et al.* [65]. Agreement with experiment is quite satisfactory. Similar to the case of the Cu TEY from Cu films, the calculated result appears to overestimate the attenuation power of Cu at higher film thicknesses. However, the large scatter in the experimental data makes the derivation of quantitative conclusions about the rôles of secondary electrons, LMM electrons and straggling difficult.

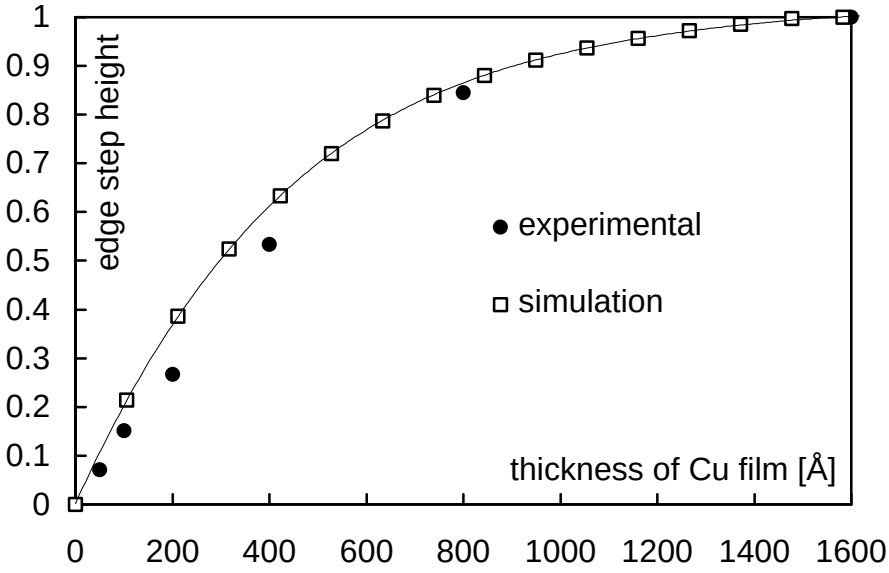

Figure 3.12. He gas-flow signal attenuation function for the Cu K-edge TEY of metallic Cu (open squares) compared to experimental signal attenuation results for Cu films deposited on quartz [101]. The line represents a 4th order polynomial fit to the simulation results. Every simulated datapoint represents the evaluation of 10,000 trajectories.

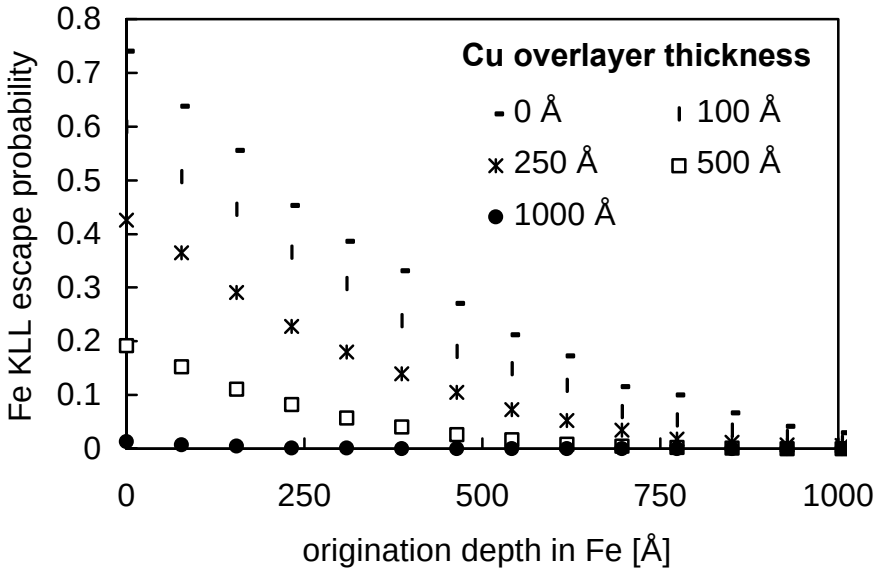

Figure 3.13. Calculated Fe KLL DDFs from a bulk Fe sample for several Cu overlayer thicknesses (see inset for explanation of symbols). Each datapoint represents the evaluation of 5000 trajectories.

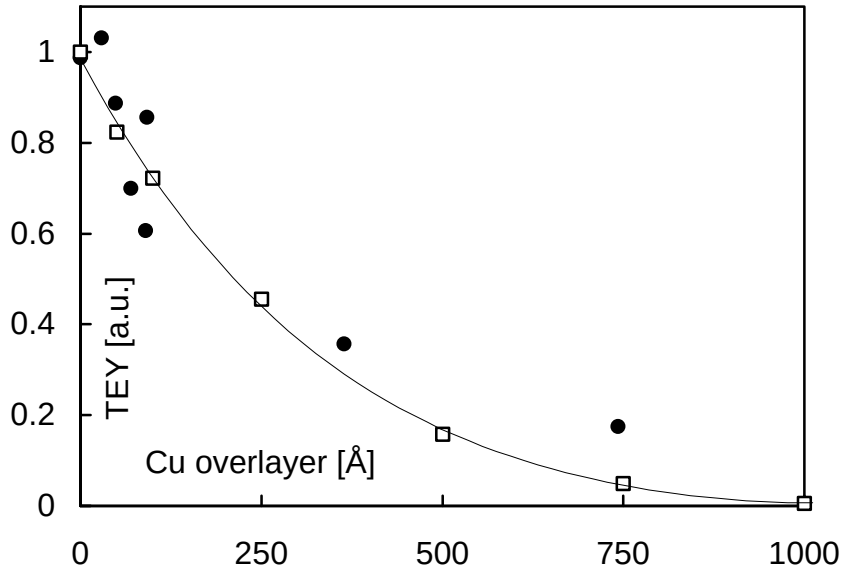

Figure 3.14. Fe K-edge attenuation calculated using 3rd order polynomial fits to the Fe KLL DDFs given in fig. 3.13. Black filled circles: experimental data. Open squares: simulated results.

3.8.3. Buried Layers: TEY Signal Attenuation in Si and Al

Erbil *et al.* and Elam *et al.* have, respectively, measured the K-edge signal from 100 Å thick films of Ge and Fe as a function of Si and Al overlayer thickness [7]. Because the experimental results [7] were in both cases reported in units of electrons per absorbed photon they allow a quantitative test of the assumption inherent in the model that secondary electron contributions to the TEY are small. The Monte-Carlo algorithm used for the simulation of the TEY signal from these systems was adapted to account for the buried-interface geometry which represents a trilayered sample.

The simulation of the Si/Ge system was carried out including the Ge KLL (8.5 keV) and Ge LMM (1.1 keV) Auger electron contributions. Agreement between experimental and calculated results was found to be excellent (fig. 3.15.): the simulation reproduces the strong initial attenuation of the Ge LMM emission by Si overlayer thicknesses up to about 200 Å. The less surface-sensitive KLL emission dominates the signal at higher overlayer thicknesses. Some caution should be exercised because the incident photon flux during the Ge K-edge measurements was uncertain to within a factor of 2 [7]. This could be the reason why the simulation results tend to overestimate the signal somewhat, except for overlayer thicknesses below 200 Å and over 3000 Å (cf. inset of fig. 3.15.). The opposite result, an underestimation of the experimental figure, would be expected because amplification due to energy straggling as well as secondary electron emission and fluorescence

have been omitted from the calculations. It is therefore possible that the experimental results should be scaled up by a uniform factor between 1 and 2, a procedure which would also lead to better agreement with the calculated attenuation function.

The influence of the secondary electron contribution should be most visible for the thinnest Si overlayers, which can be penetrated by the Ge LMM electrons. The energy of these electrons coincides with the energy region where secondary electron excitation in Si and Ge is known to be most pronounced [48]. The simulation, which ignores secondary electron emission, underestimates the experimental data at the lowest Si overlayer thicknesses (fig. 3.15.). It is interesting to note that the deviation between the experimental value for zero overlayer thickness (1.1 electrons/photon) and the calculated value (0.9 electrons/photon) is compatible with secondary electron contributions of less than 50% of the TEY. Even in the unlikely case that the experimental data are uniformly too low by a factor of 2 the maximum deviation between experiment and Auger-yield simulation would be approximately 60%. The analysis therefore supports the view that secondary electron contributions are not dominating the TEY signal.

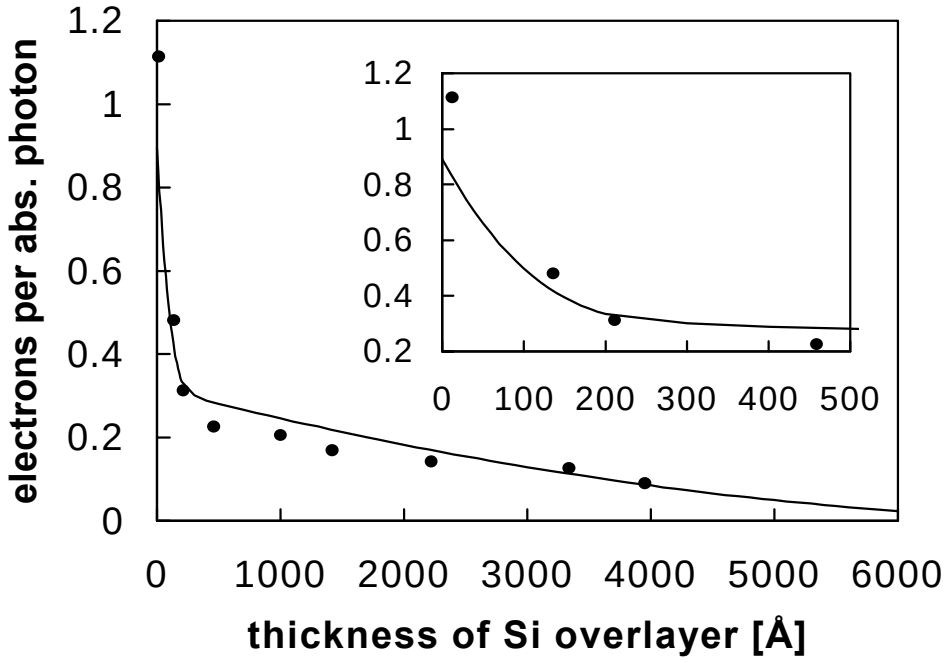

Figure 3.15. Simulated TEY signal attenuation function for the Ge K-edge absorption of a thin Ge layer buried in Si (experimental data from [7]). Ge KLL and LMM DDFs have been included in the simulations. Filled black circles: experimental data [7]. Lines: simulation results interpolated using third order polynomials. Note that the inset is simply an enlargement of the thickness region below 500 Å in the main chart.

This conclusion is also borne out by an analysis of the Fe K-edge attenuation data reported by Elam *et al.*. These authors deposited increasingly thick layers of Al on a 100 Å film of Fe and measured the resulting Fe K-edge TEY signal in vacuum. Fig. 3.16 compares their TEY data to two calculated attenuation functions. The thin line represents the result which is obtained when only Fe KLL emission (probability for radiationless decay: 0.66) is taken into account. This attenuation function clearly underestimates the absolute TEY current for all overlayer thicknesses. A much better fit to the data is obtained when it is assumed that every emitted KLL electron is accompanied by the emission of 0.5 secondary charges. Again, the largest deviations between the calculated function and the experimental figures are observed for the lowest and the highest Al overlayer thickness. At low thicknesses, Fe LMM (650 eV) electrons and concomitant secondary electrons are expected to add to the TEY. Deviations between the calculated attenuation function and the experimental datum for the thickest film (2200 Å) occur presumably for the same reasons (straggling, film inhomogeneity, secondary electrons) as previously discussed for the Cu films. It should also be kept in mind that the data of Elam *et al.* were obtained by the same method as the data of Erbil *et al.*, so that it is possible that the error margins of the electron currents per photon flux are substantial. Nevertheless, the fact that overall agreement with experimental data is achieved by assuming that 2/3 (66.6%) of the TEY are KLL Auger electrons does also support the view that the secondary yield fraction is lower than previously assumed. Unfortunately, no results have been

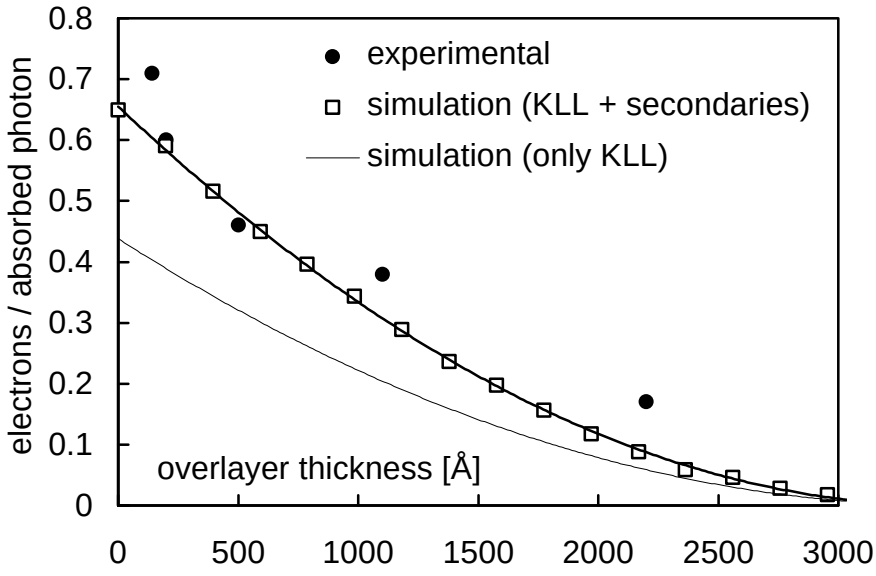

Figure 3.16. Attenuation of the vacuum TEY signal from a 100 Å layer of Fe buried under an increasingly thick Al overlayer. Filled circles: experimental data of Elam *et al.*; open squares: simulated attenuation curve based on Fe KLL emission. Note that both experimental and calculated results are in absolute units of electrons per absorbed photon. Every calculated datapoint represents the evaluation of 10000 trajectories.

reported for very low Al overlayer thicknesses which would allow a more quantitative assessment of the influence of the Fe LMM emission.

3.8.4. TEY Signal Attenuation in the Soft X-ray Range

The Ta_2O_5/Ta and Al_2O_3/Al systems are interesting benchmarks to the model claculations because they involve (i) compounds and (ii) soft absorption edges. They provide therefore a simultaneous test of Browning's algorithm at low electron energies and of Bragg's rule. The analysis of the vacuum TEY attenuation functions has been made in terms of the oxide signal in the KLL spectra at the Al K-edge (1.56 keV, *vide infra*) and the O K-edge (0.5 keV, fig. 3.17).

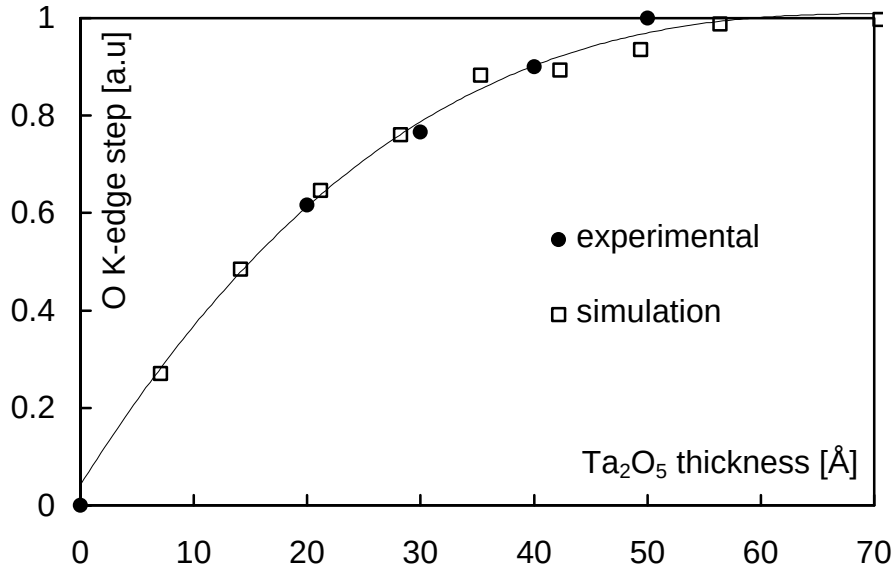

Figure 3.17. O K-edge signal from Ta_2O_5 overlayers supported on Ta as a function of oxide overlayer thickness. Filled circles: experimental vacuum data; open squares: calculated O KLL data (every datapoint represents the evaluation of 5000 trajectories). The full line represents a 4th order polynomial fitted to the calculated data.

Fig. 3.17. shows that the calculated result for Ta_2O_5 overlayers is in excellent agreement with experimental data [9]. This result could be taken as evidence that the present Auger yield calculations are a good model for the TEY even in the soft X-ray range, despite the uncertainties introduced by using a CSD approximation at very low energies (see also section 3.7). However, it is also found that the simulations achieve poor agreement with soft X-ray data for the attenuation of the Ni L_3-edge (0.85 keV) signal by rare earth overlayers [9,10]. Fig. 3.18. shows that the Ni LMM simulation severely overestimates the mass attenuation of the Ni L_3-edge signal in Dy by more than a factor of 2. This result cannot be explained by the influence of secondary

electron production, straggling, or film porosity, as all these factors could only increase the depth probed by the TEY signal. The origin of the large discrepancy therefore remains unknown. Electron scattering at the overlayer/substrate interface or the formation of an unusually dense phase of Dy might be responsible for the strong attenuation of the TEY. The disagreement with experiment could also be related to the limits of the CSD approximation, as the shallow 4f core levels of rare earths could have quite large electron impact ionisation cross sections, increasing the stopping power significantly. On the other hand, unusually strong electron attenuation characteristics have never been noticed in surface science studies of rare earth overlayers [104-108]. More work is required to clarify the situation here. In the meantime, caution is advisable when the present Monte Carlo simulation model is applied in the soft X-ray range.

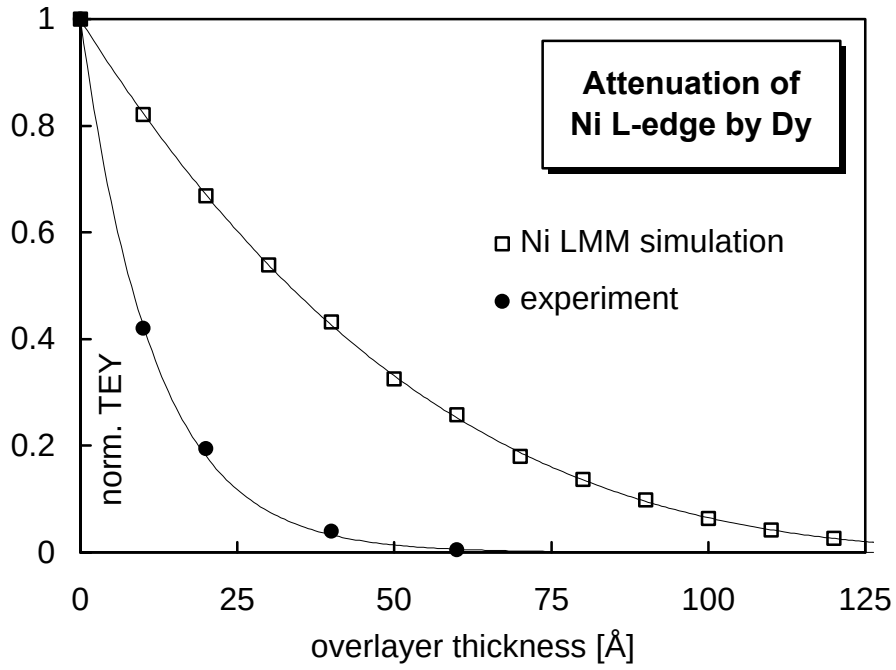

Figure 3.18. Ni L_3-edge signal attenuation by Dy overlayers. Filled circles: experimental data, open squares: simulation results.

The calculated thickness dependence of the TEY signal from Al_2O_3 overlayers grown on Al (fig. 3.19) reproduces the growth of the oxide signal with similar accuracy as previous phenomenological analyses [7,63-65]. Quantitative comparisons between simulation and experiment are made difficult by the fact that the accuracy of the experimental data is considerably uncertain [109].

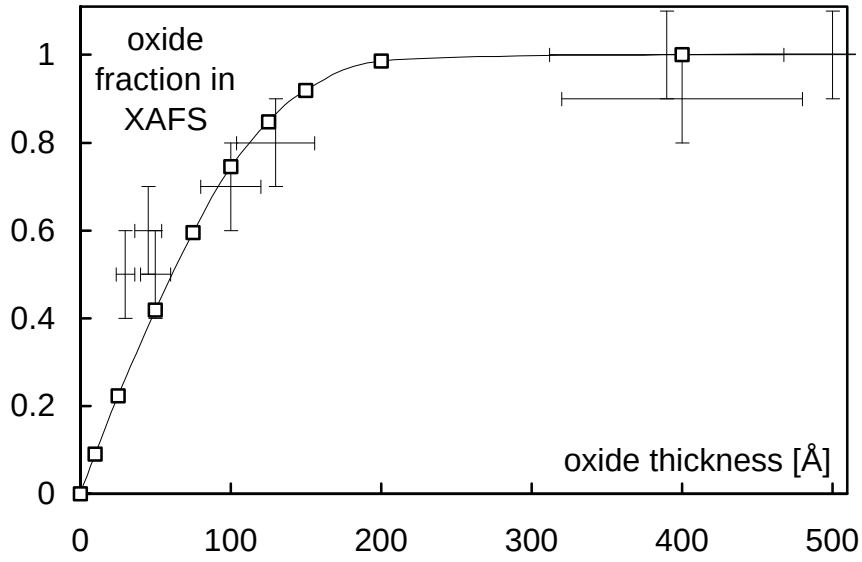

Figure 3.19. Simulated (Al KLL electrons, open squares) and measured (error bars) dependence of the oxide fraction in the vacuum Al K-edge signal from samples consisting of Al_2O_3-covered Al (a correction has been applied to account for the lower density of Al absorbers in the oxide). The error bars have been estimated by inspection of the results given in refs. [63,64].

Nevertheless, the analysis of the TEY signal attenuation in Al and Al_2O_3 yields some interesting results. Jones and Woodruff suggested that a longer inelastic mean free path (IMFP) of the signal electrons lengthens their penetration range in the oxide relative to the metal. They fitted an exponential model to the data assuming attenuation lengths of 65 Å for Al and 130 Å for Al_2O_3 [63]. The picture emerging from the present work is that the penetration of Al KLL electrons in Al_2O_3 is actually more limited and that the previously suggested attenuation lengths of 65 Å and 130 Å over- and underestimated the backscattering ability of Al and Al_2O_3, respectively (fig. 3.20). An explanation for the discrepancy between the two interpretations emerges from examination of the elastic mean free paths (calculated with equations (3.14) and (3.20)) and the stopping powers (equations (3.18) and (3.19)) for the two materials (fig. 3.21). At all energies, the former is shorter and the latter is larger in the oxide, favouring a high degree of backscattering from Al_2O_3. Qualitatively, this result seems reasonable because the density of Al atoms in Al_2O_3 is 76% of that in Al metal and the presence of 1.5 additional O scatterers per Al atom should lead to higher scattering and energy-loss cross sections in the oxide. This interpretation is supported by more elaborate calculations of elastic scattering cross sections reported elsewhere [98]. Some caution must be exercised when interpreting the stopping powers given in fig. 3.21 because of the lower reliability of the CSD approximation at these low energies (see section 3.7). Additional uncertainty relates to the

application of Bragg's rule in the calculation (*vide infra*), but the trends seen in fig. 3.21 are most probably correct.

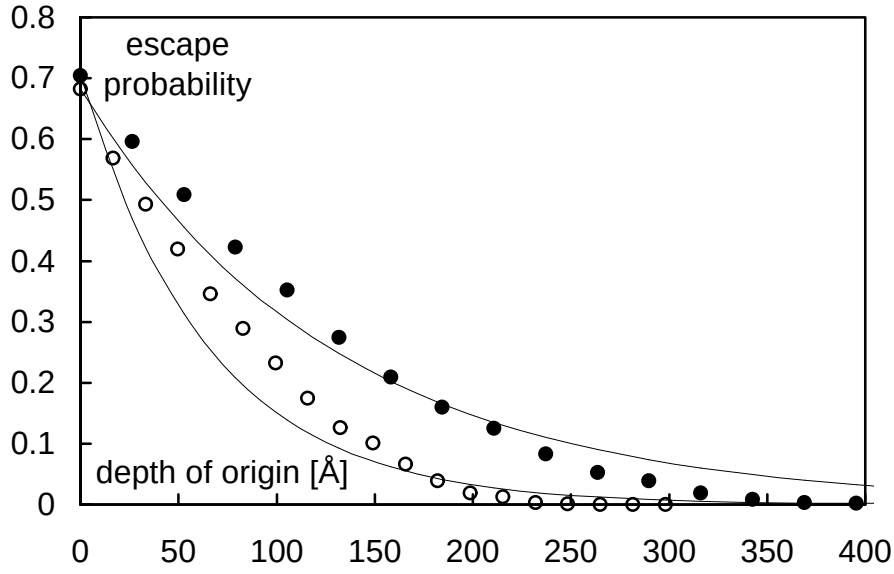

Figure 3.20. Depth distribution functions for Al KLL electrons emitted from metallic Al (filled circles) and Al_2O_3 (open circles). The full and dashed lines show previously derived [63] exponential attenuation functions for Al and Al_2O_3, respectively.

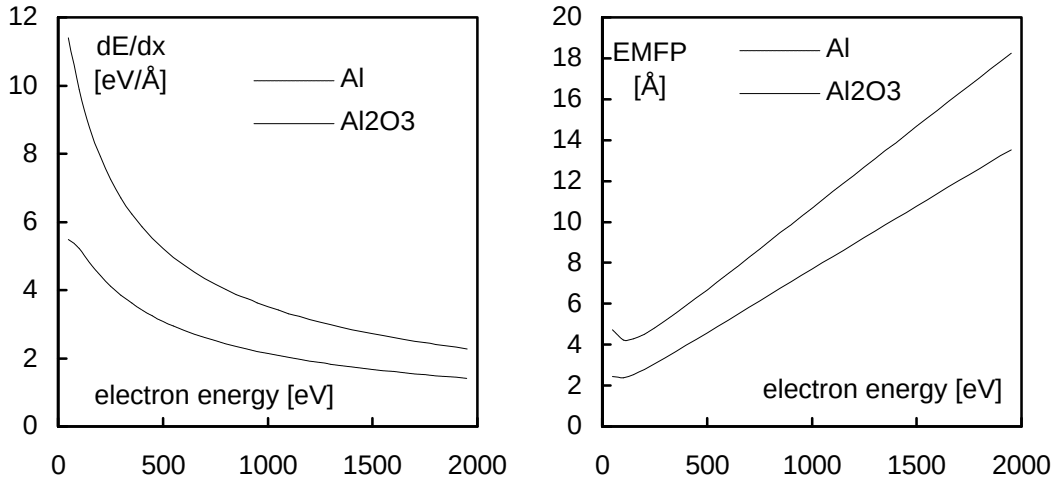

Figure 3.21. Stopping powers and elastic mean free paths (EMFP) as used in the simulations of the Al K-edge results. Left chart: stopping powers. Right chart: elastic mean free paths. Al_2O_3 data are indicated by full lines and Al data by dotted lines.

It appears that Jones and Woodruff [63] were misled in their analysis because they extrapolated from IMFP values measured at very low electron energies [110]. These measurements were carried out at energies below 100 eV and indicated that the IMFP in Al_2O_3 is longer than in Al by a factor of about 2. However, the IMFP difference between both materials becomes small at higher electron energies [103,111], and it is

well known that the average energy loss per unit path is substantially higher in Al_2O_3 than in Al. The latter is very clearly borne out by the dielectric loss functions of both materials [111,112]. These reveal that a higher plasmon energy enhances the stopping power of Al_2O_3.

A final note shall be added to discuss the error which might have been introduced in the calculations by assuming additivity of the elemental stopping powers in Al_2O_3 (and Ta_2O_5). Deviations from the additivity rules expressed in equations (3.18) and (3.19) are expected at low electron energies, and when chemical bonding influences a large proportion of the total number of electrons in the constituent atoms. Low-Z atoms which exhibit a high fraction of valence electrons, are particularly prone to chemical bonding effects, making the prediction of exact stopping powers difficult for their compounds. An error can be introduced *via* the mean ionisation potential J_c calculated using Bragg's rule, cf. eq. (3.19). Experimental determinations of the mean ionisation potential of Al_2O_3 have been described in the literature, but the exact value remains controversial [97,113]. The quoted experimental values range from 123 eV [97] to 145 eV [94], while application of Bragg's rule yields values between 120 eV and 135 eV, depending on the choice of J_i for the constituent elements [89,97]. It has been found that additivity-based predictions of J_c for low-Z compounds are often lower than measured values, an observation which has led to the proposal that a correction factor of 1.13 should always be applied to values calculated by equation (3.19) [89]. The value used in the present simulations was 133 eV, so that application of this '13% rule' would result in a figure of 150 eV. The maximum error introduced by the choice of different J_c can be estimated by calculating the total range of a 1.4 keV electron *via* numerical integration of equation (3.18). The range of J_c-values which appear physically justifiable was estimated to be between 120 eV and 150 eV. The corresponding electron ranges vary by less than 10% with respect to the range determined for 135 eV, indicating that the error introduced into the Monte-Carlo simulation is unlikely to be larger than other errors intrinsic to Browning's algorithm.

3.9. The Probing Depth Difference between Total Electron-Yield Detection in Vacuum and in Gas-Flow Mode. II. Data Analysis

Having established a method for the calculation of TEY signals in vacuum and in gas-flow mode, we can now proceed to interpret the attenuation data from section 3.3. in a more quantitative manner. Figures 3.22. and 3.23. present, respectively, the calculated DDFs for the Ni KLL and Ni LMM attenuation in Ni and NiO. It is seen

that the Auger electron attenuation power of NiO is generally weaker than in Ni metal. This is mostly a result of the lower mean ionisation potential of NiO which decreases the electron stopping power relative to Ni: Bragg's rule predicts a J_c value of 240.7 eV for NiO, while the corresponding figure for Ni metal is 304.3 eV.

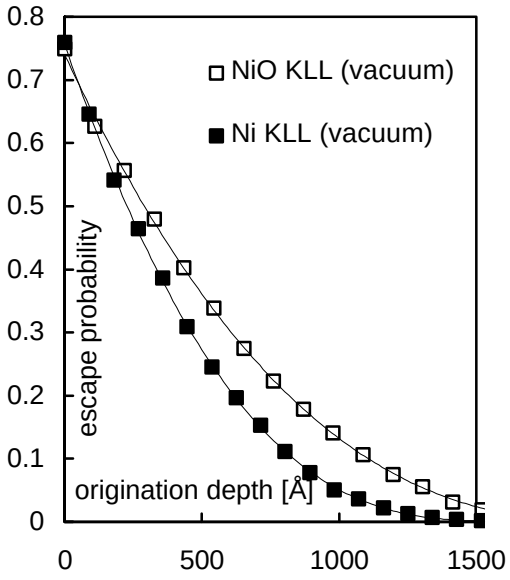

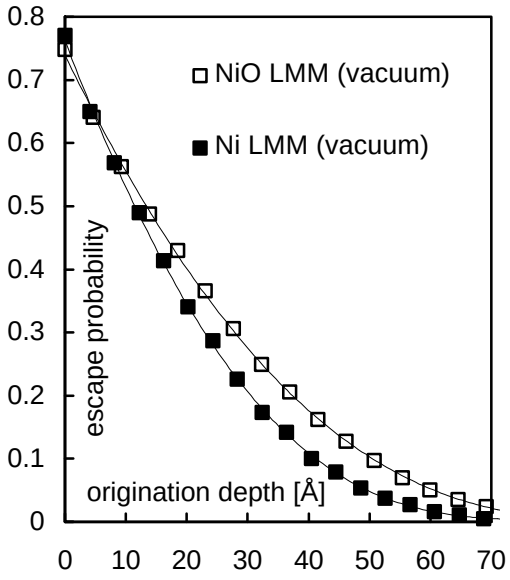

Figure 3.22. (left) Depth distribution functions for the Ni KLL (6.5 keV) attenuation in Ni metal and NiO. Each datapoint represents the evaluation of 10,000 trajectories.

Figure 3.23. (right) Depth distribution functions for the Ni LMM (0.85 keV) attenuation in Ni metal and NiO. Each datapoint represents the evaluation of 10,000 trajectories.

The effect of gas-phase amplification on the KLL emission is illustrated in figure 3.24. The surface sensitivity of the KLL yield decreases by weighting the signal towards high-energy contributions. The simulated KLL emission spectra (not shown, as the spectra look very similar to those given for Cu in fig. 3.7) indicate further that gas phase amplification in He increases the signal intensity of the KLL yield by factors of 117 and 116 for Ni and NiO, respectively. These figures suggest that the average KLL electron energy is in the vicinity of $116 \times 42\ \text{eV} \approx 4.9\ \text{keV}$. For comparison, the calculated amplification factor for the Ni LMM emission from Ni and NiO is 14 for both materials, corresponding to an average LMM energy of approximately 580 eV. Gas phase amplification thereby diminishes the relative weight of the LMM contribution to the TEY signal by about an order of magnitude. This result supports the conclusion drawn in section 3.3 that the LMM contribution to the gas-flow signal is insignificant compared to vacuum detection.

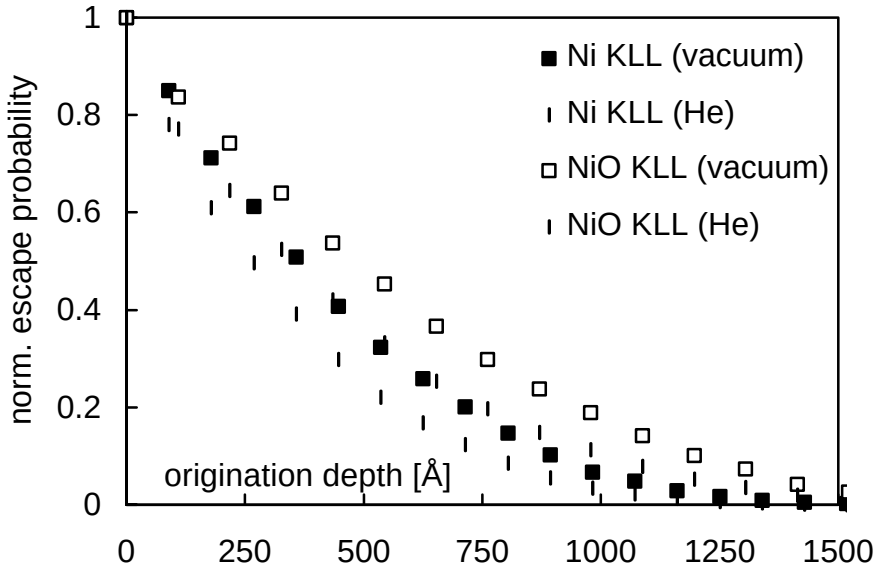

Figure 3.24. Normalised depth distribution functions for the Ni KLL (6.5 keV) signal from Ni metal and NiO as detected in vacuum and in a He filled TEY detector. Note the effect of gas-phase amplification on the depth information which results in an enhancement of the surface sensitivity of the KLL yield.

The analysis of the NiO/Ni data presented in section 3.3. requires a knowledge of (i) the attenuation of the Ni metal TEY as a function of NiO overlayer thickness, and (ii) the concomitant increase of the NiO TEY. The Auger yield signals of both sample components have been calculated from the simulated DDFs using equations (3.3) to (3.9). The probabilities for radiationless decay of Ni K- and L-holes are a_{KLL} = 0.594 and a_{LMM} = 0.99, respectively [16]. The K_a/K_b emission rate ratio is 0.135 [67] and the K-shell fluorescence decay probability w_K is 1 - a_{KLL} = 0.406 [16]. The analysis has to take into account that the number density of Ni emitters in NiO is $5.38 \cdot 10^{22}$ cm^{-3} as compared to $9.13 \cdot 10^{22}$ cm^{-3} in Ni metal. As a result, the rate of Ni Auger electron production per unit volume of NiO is only ≈ 59% of the rate in Ni.

The integration of the vacuum DDFs for the KLL and LMM emission from Ni metal and NiO as a function of oxide overlayer thickness (the DDFs are not shown, as they are qualitatively very similar to those given for the Fe K-edge attenuation by Cu, see fig. 3.13) yields the attenuation functions presented in figures 3.25 and 3.26. Based on these functions, the evolution of the NiO fraction in the vacuum TEY XAFS as a function of overlayer thickness can be predicted. Figure 3.27. compares the resulting attenuation function and experimental data (as summarised in table 3.1. in section 3.3.). It is immediately obvious that the Auger yield calculation

underestimates the NiO contribution to the XAFS at all overlayer thicknesses over approximately 200 Å.

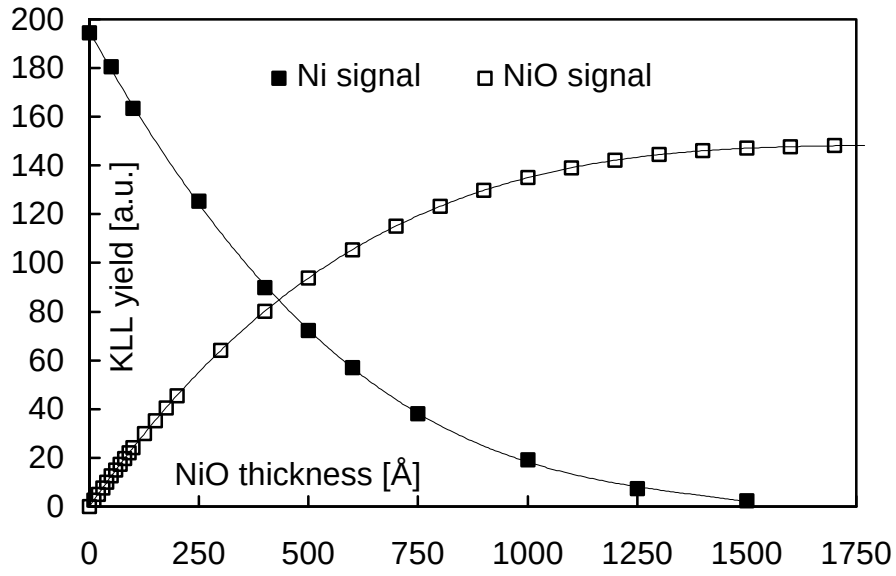

Figure 3.25. Integrated Ni metal and NiO KLL yield as a function of NiO overlayer thickness.

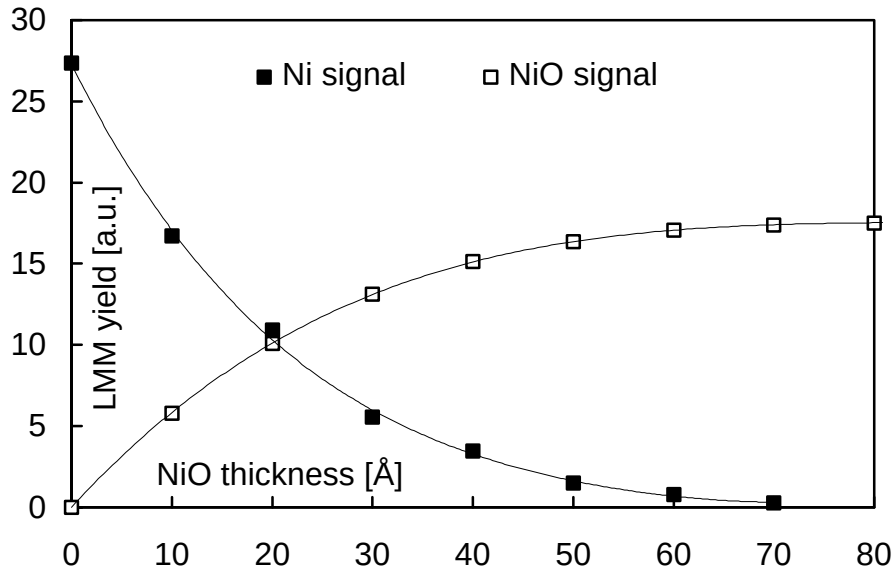

Figure 3.26. Integrated Ni metal and NiO LMM yield as a function of NiO overlayer thickness.

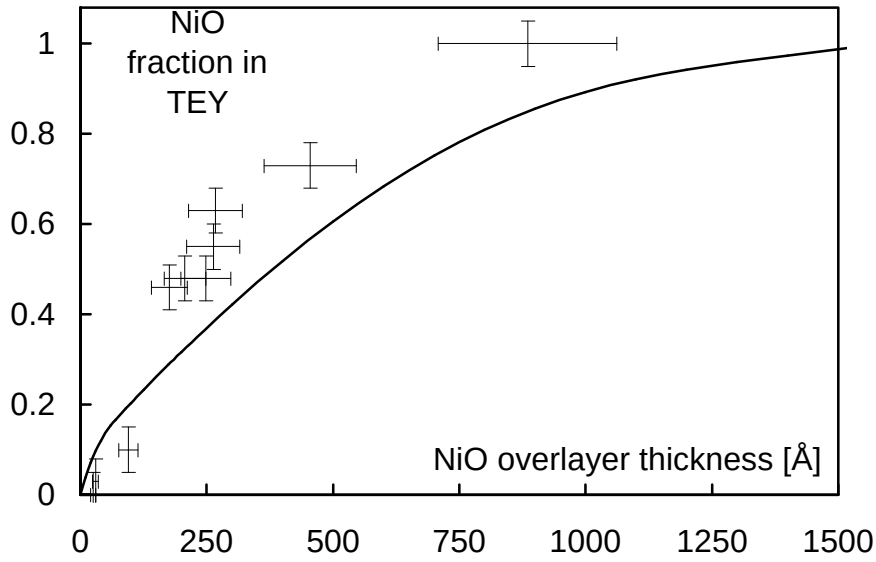

Figure 3.27. Calculated NiO contribution to the vacuum TEY XAFS (full line) as a function of NiO overlayer thickness. Crosses with error bars: experimental data. The calculation was carried out neglecting the contribution of secondary electrons entirely.

The reason for the discrepancy between experiment and theory is likely to be the neglect of secondary electron contributions to the vacuum TEY. Several factors are expected to enhance the secondary electron contribution from NiO covered Ni wafers relative to a clean Ni metal surface. Firstly, the secondary electron yield from insulators is generally larger than from metallic sample specimens [23,47] because of the longer escape depth for low-energy electrons. The conduction band of insulators is close to or above the vacuum level, so that the cross sections for energy losses are small and the attenuation of low-energy electrons is less efficient than in a conductor. Secondary electron yield contributions of 99% and more have experimentally been observed for some insulators, most notably CsI [28,29]. Another contributing factor is the presence of voids and microroughness in/on the NiO overlayers, as revealed by the ellipsometric analysis of the NiO morphology *via* effective medium approximations (see Appendix A). The mechanism which might be responsible for an enhancement of the secondary electron yield from a rough surface is illustrated in fig. 3.28. Randomly oriented NiO crystallites on the surface allow the escape of secondary electrons from facets with an orientation inclined with respect to the macroscopic sample surface. This effect is well known and has been analysed theoretically (cf., e.g., [114]). Its enhancing influence on the secondary electron current should be particularly pronounced when the oxide overlayer grows in a dendritic fashion - as often observed in electron microscopic images of NiO scales grown on Ni wafers [115,116].

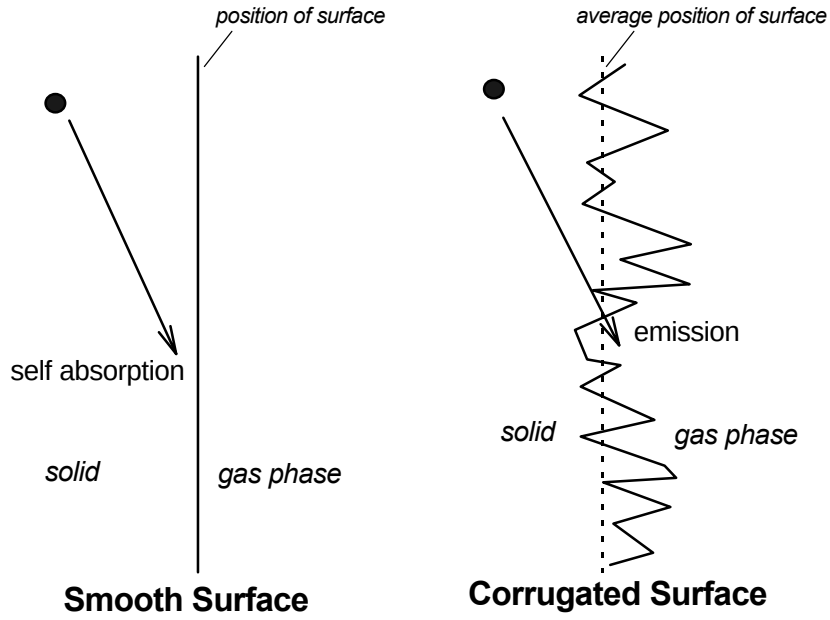

Figure 3.28 Influence of surface roughness on the probability for the emission of a secondary electron (represented by a filled circle) travelling along a trajectory (arrow) with a low incidence angle with respect to the macroscopic sample surface plane.

Finally, it should also be kept in mind that some charging of the insulating overlayer is likely to occur in a vacuum TEY experiment. Accumulation of positive charge at the surface of thin, insulating overlayers is a common problem in electron microscopes [23]. Its effect on the secondary electron emission derives from the decrease of the surface potential barrier, permitting the escape of a larger number of secondary electrons. Thin film charging has been estimated to enable, in some cases, a more than 4-fold increase of the secondary electron current from samples covered by insulating overlayers [47].

The effect of an increased secondary electron contribution to the TEY should be observed experimentally as a decrease in the gas phase amplification factor. Figure 3.29 summarises the experimentally determined dependence of the gas phase amplification factor on the thickness of the NiO overlayers. It is clearly seen that the amplification does indeed decrease by approximately 50% as the NiO overlayer thickness reaches 200 Å. For higher NiO thicknesses, the amplification factor assumes a constant value of approximately 45. It is currently difficult to decide which mechanisms contributes to the enhancement of the secondary yield from NiO-covered samples. However, the Monte-Carlo simulation results allow to derive an estimate of the actual fraction of secondary electrons in the TEY. This is achieved by balancing the magnitude of the individual contributions to the TEY as follows.

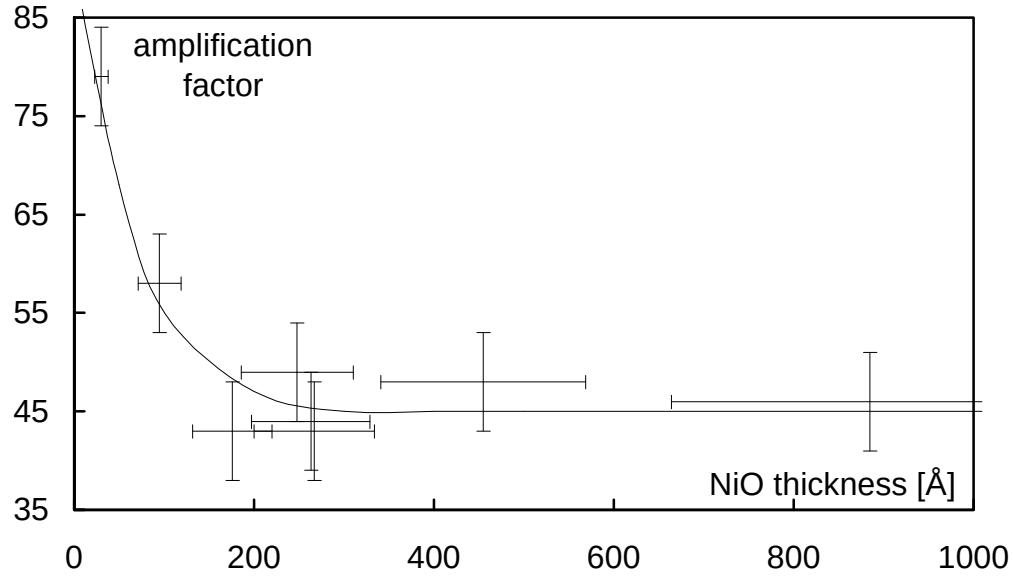

Figure 3.29. Dependence of the gas phase amplification factor on the NiO overlayer thickness. See text for the discussion of this figure. The line through the data has been drawn to guide the eye. Crosses with error bars: experimental data.

The measured gas phase amplification factor A_{obs} must derive from the multiplication of KLL and LMM charges emitted from the sample. Amplification of Ni MVV electrons is insignificant, because of their very low kinetic energy (≈ 60 eV), so that they can be subsumed under the non-amplifiable fraction of true secondary electrons. The simulations provide (i) the amplification factors A_{KLL} and A_{LMM} for the KLL and LMM contributions, respectively, and (ii) the relative intensities of the Auger electron fluxes from the KLL- (i_{KLL}) and LMM-channels (i_{LMM}) (see figures 3.25 and 3.26). The magnitude of the secondary electron flux i_{sec} is unknown. The TEY observed in vacuum is the sum of all three flux contributions,

$$TEY = i_{KLL} + i_{LMM} + i_{\mathrm{sec}}, \quad (3.23)$$

while the gas-flow signal is given by

$$A_{obs} \cdot TEY = A_{KLL} \cdot i_{KLL} + A_{LMM} \cdot i_{LMM} + i_{\mathrm{sec}}. \quad (3.24)$$

Dividing the two signal intensities yields the secondary yield i_{sec} as a function of the observed amplification factor:

$$A_{obs} = \frac{A_{KLL} \cdot i_{KLL} + A_{LMM} \cdot i_{LMM} + i_{\mathrm{sec}}}{i_{KLL} + i_{LMM} + i_{\mathrm{sec}}} \quad (3.25a)$$

$$\Leftrightarrow \qquad i_{\mathrm{sec}} = \frac{(A_{KLL} - A_{obs}) \cdot i_{KLL} + (A_{LMM} - A_{obs}) \cdot i_{LMM}}{A_{obs} - 1}. \quad (3.25b)$$

The secondary electron fraction in the TEY is then given by

$$i_{\mathrm{sec}}\,[\%] = \frac{i_{\mathrm{sec}}}{i_{KLL} + i_{LMM} + i_{\mathrm{sec}}} \cdot 100\% \,. \qquad (3.26)$$

This function is evaluated in figure 3.30 for Ni and NiO over a wide range of amplification factors. Comparison with figure 3.29 indicates that the secondary yield fraction in the TEY increases from approximately 20% ($A_{obs} \approx 85$) for a polished Ni metal surface to about 60% ($A_{obs} \approx 45$) for the Ni wafers covered by thick NiO overlayers.

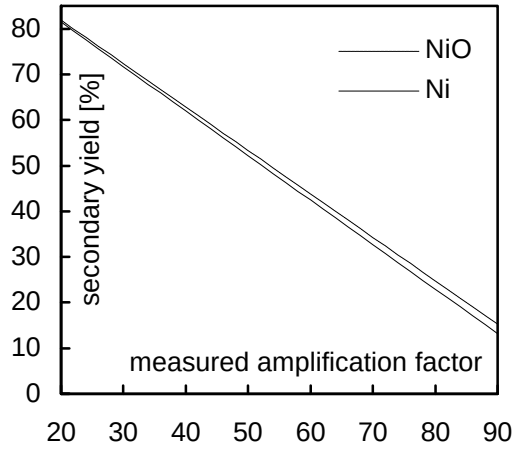

Figure 3.30. Dependence of the secondary electron yield contribution to the TEY on the gas phase amplification factor. See text for the model underlying the calculations. Parameters: Ni: $i_{KLL} = 197$, $i_{LMM} = 27.5$, $A_{KLL} = 116$, $A_{LMM} = 14$. NiO: $i_{KLL} = 147.8$, $i_{LMM} = 17.7$, $A_{KLL} = 117$, $A_{LMM} = 14$.

Most of the secondary electron yield is expected to derive from inelastic interactions of the LMM cascade (E = 0.85 keV) because of the high cross sections for energy losses at kinetic energies below 1 keV. The penetration range of the Ni LMM electrons in NiO is comparable to or shorter than the thickness of the near surface region from which the secondary electrons escape, so that it is likely that each LMM electron generates several secondary charges. Indeed, if one assumes that secondary electron production weights the depth information in the TEY four times towards the LMM- over that of the KLL contributions (fig. 3.31), then much better agreement between calculation and experiment is achieved than for the pure Auger yield model (fig. 3.27). However, this *ad hoc* modification of the model by use of a constant factor is only of limited value, as it neglects the energy dependence of the secondary yield production rate. Furthermore, it does not take account of the fact that the LMM yield at low NiO overlayer thicknesses originates mostly in the Ni substrate. As a result, the experimental NiO fraction in the TEY is much lower than predicted by the simulation. The modification nevertheless illustrates the fact that the internal signal amplification due to secondary electron production can be important for vacuum TEY experiments. The influence of the secondary yield from the NiO/Ni samples is much more pronounced than in any of the systems analysed in section 3.8. because of the unique properties of the thin, insulating overlayers.

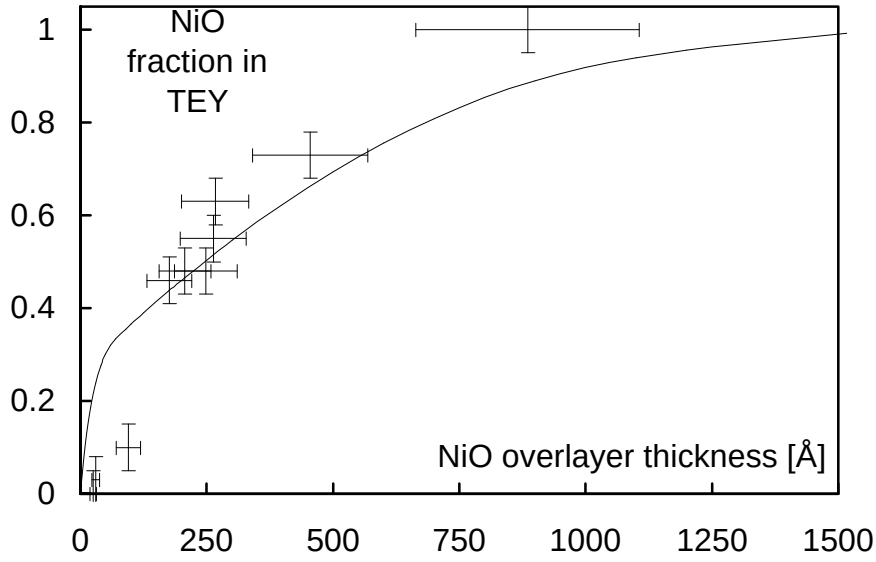

Figure 3.31. Calculated NiO contribution to the vacuum TEY XAFS (full line) as a function of NiO overlayer thickness. The calculation was carried out as in fig. 3.27, except for weighting the LMM contribution to the TEY four-fold to model the influence of secondary electron production.

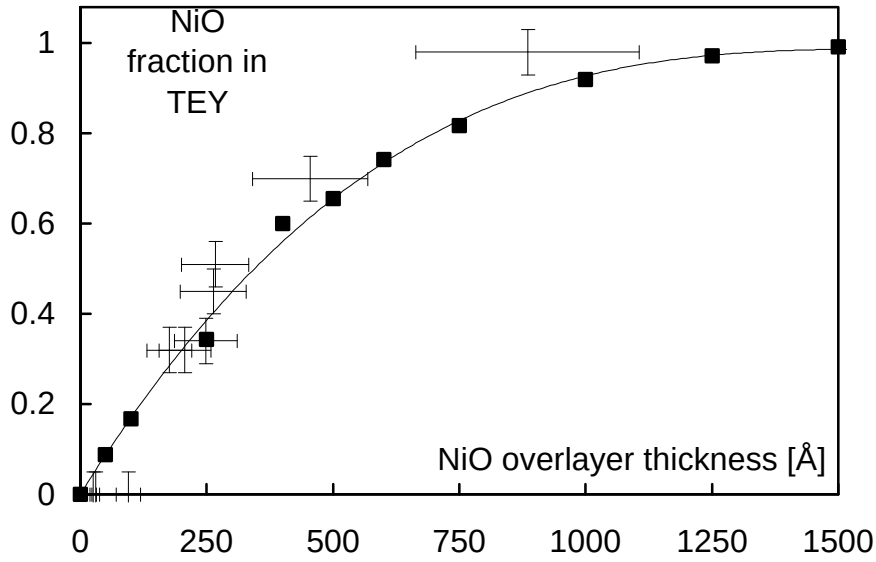

Figure 3.32. Calculated (full line, black squares) and experimental (crosses with error bars) NiO contributions to the He-flow TEY XAFS as a function of NiO overlayer thickness. LMM and secondary electron contriutions to the TEY were entirely neglected in the calculation.

Gas phase amplification must reduce the influence of the secondary electrons in gas-flow detection mode. In line with this prediction, a Monte-Carlo analysis of the He-flow data in terms of the KLL emission affords very satisfactory agreement with experiment (fig. 3.32). The calculated result still appears to underestimate the NiO contribution somewhat for higher NiO thicknesses, the reason probably being the neglect of the residual influence of LMM- and secondary electrons. The overall much

better agreement of the pure Auger yield model with gas-flow than with vacuum data is reassuring evidence that the depth distribution functions calculated by Browning's Monte-Carlo simulation method are quite accurate.

3.10. Towards a 'Universal Curve' for Total Electron-Yield XAS

The DDFs for the KLL emission (energy range: 1 keV - 26 keV [40]) from all 40 solid elements between Na and Ba (excluding Tc) were calculated using the Monte-Carlo trajectory simulation algorithm described in section 3.7. Figure 1 displays a representative selection of simulation results, covering the elements between K and Zn (KLL energies: 2.96 keV to 7.49 keV [40]). The escape probability for electrons originating at the surface is in all cases approximately 0.75, indicating that elastic scattering redirects 50% of the electrons emitted towards the sample volume back through its surface. The data also show that the KLL penetration does not follow a

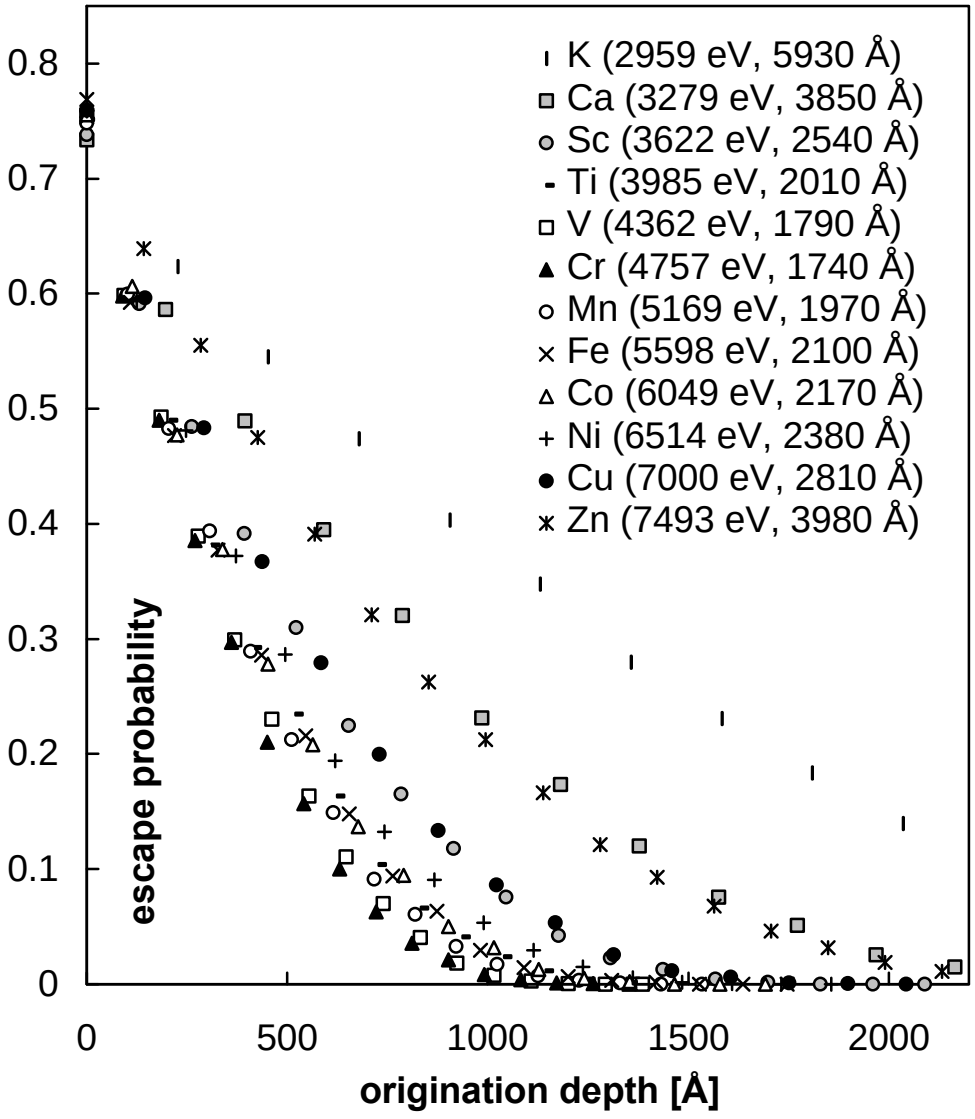

Figure 3.33. Calculated depth distribution functions for the KLL emission from the 12 elements listed in the inset (the values in brackets are the KLL electron energies in eV and the Bethe ranges in Å).

monotonically increasing trend of escape probability with electron energy, as illustrated by the case of K which represents the lowest Auger electron energy (2.96 keV) yet exhibits by far the largest KLL electron penetration among the elements included in fig. 3.33. Obviously, material parameters, particularly the density, play an important rôle in determining the electron penetration characteristics. It has been shown in a related context [117] that the Auger electron attenuation function is only weakly material-dependent when the electron origination depth is expressed as a fraction of the total electron range (defined as the total path length travelled by an electron in a solid before it has dissipated all its kinetic energy). The total range, often [7] referred to as the 'Bethe range', R_B, can be calculated by numerical integration of equation (3.27),

$$R_B = \frac{M}{785 \cdot r \cdot Z} \int_{E_0}^{40eV} \frac{E}{\ln\left(J / [1.166 \cdot (E + t \cdot J)]\right)} dE\,, \quad (3.27)$$

between the initial electron energy E_0 and the low-energy cut-off as applied in the trajectory simulations (see also section 3.7). The inset of figure 3.33 gives calculated R_B values. The expression of the electron origination depth, *x,* in units of R_B

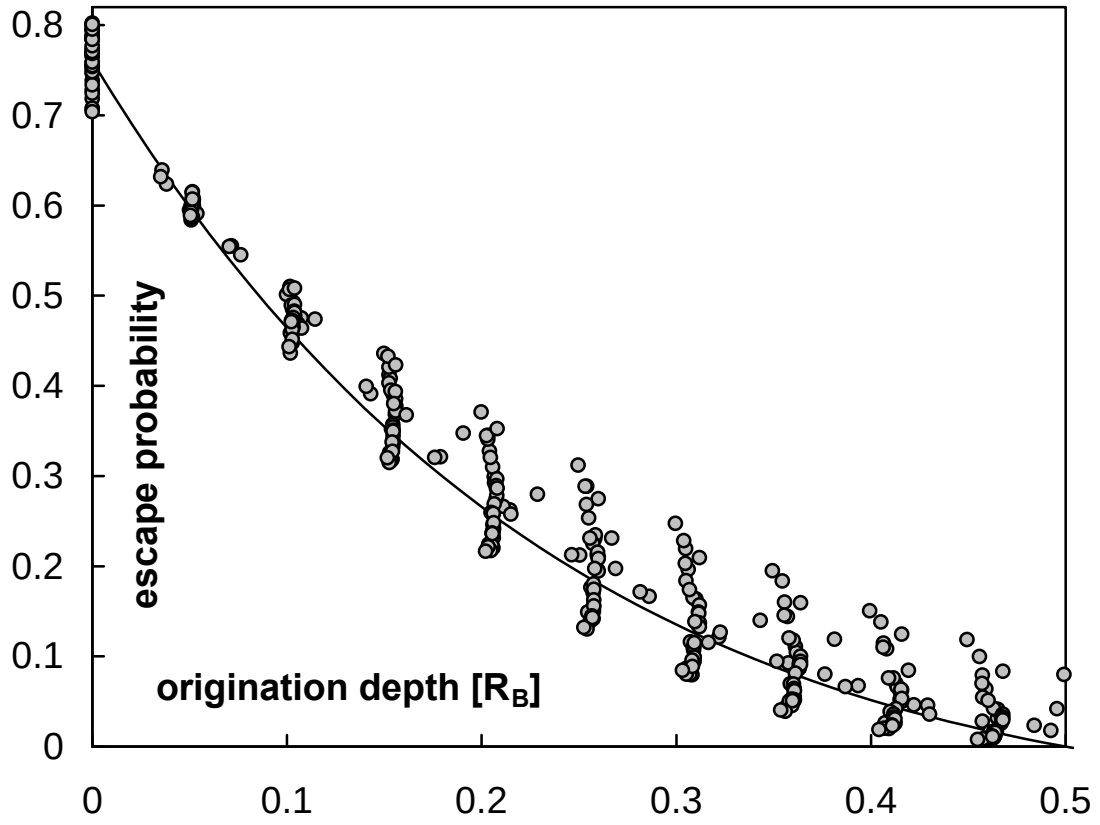

Figure 3.34. Depth distribution functions (DDFs) for 40 elements expressed as a function of the total electron range ('Bethe range') R_B. The full line represents the 'universal DDF' described in the text.

superimposes all 40 calculated DDFs onto a common plot (figure 3.34) and shows that scattering limits the Auger electron penetration to approximately 0.5 R_B for all 40 elements. The function

$$P(x) = 0.76 \cdot (1 - 2 \cdot x/R_B) \cdot \exp(-2.7 \cdot x/R_B) \quad (3.28)$$

describes the collection of 40 calculated DDFs quite accurately (fig. 3.34), and is in good agreement with a result obtained by analysing a much more limited database of calculated attenuation data [117]. Closer examination of this 'universal' DDF reveals that it underestimates the electron penetration in low-Z (Z < 16) materials by about 10% - 20% (all datapoints far above the fitted curve in fig. 3.34 derive from simulations involving the elements between Na and S). For all other elements considered in this study equation (3.28) was found to be a good representation of calculated DDFs at electron energies down to about 0.8 keV. Note that the 'universal' DDF becomes negative, and therefore physically meaningless, for origination depths larger than 0.5 R_B.

As discussed in section 3.5., earlier workers [9,10,65] have employed exponential functions of the form $P(x) \mu \exp(-x/l)$ for the description of TEY attenuation data. This approach has the advantage that the decay constant l can be interpreted conveniently as the probing depth of the TEY signal, thereby defining the probing depth as the thickness of the near-surface region from which the fraction 1 - 1/e (63.2%) of the emitted signal originates. However, the *a priori* choice of an exponential attenuation function is physically difficult to justify, especially in view of the strong experimental evidence for non-exponential TEY signal attenuation (see previous sections and [7,102]. Indeed, the calculated Auger electron DDFs in figures 3.33 and 3.34 do not have a simple exponential form. Maintaining the 63.2% boundary definition would yield a value of 0.149 R_B for the probing depth predicted by equation (3.28). However, it must be borne in mind that the TEY signal has contributions from several radiationless decay channels, so that the TEY is the sum of contributions due to higher- (e.g., KLL) and lower-energy (e.g., LMM) Auger electron emission. It is therefore more meaningful to apply the 63.2% definition to the sum of calculated Auger yield DDFs relevant for each absorption edge and material. Assuming that the attenuation length for X-rays is much longer than the Auger electron escape depths, the flux of Auger electrons $i(d)$ emitted from a film of thickness d is given by [7]

$$i(d) = I_0 \cdot \sum_i n_i \cdot \int_0^d P_i(x) \cdot dx \,, \quad (3.29)$$

where I_0 is the incident flux of X-rays, and n_i denotes the correction factor necessary to account for varying Auger decay probabilities and vacancy multiplication in the Auger cascade (see section 3.5 and [7]). The summation is carried out over all Auger channels (KLL, LMM, etc.) involved.

A total Auger yield attenuation function derived using this simple approach shall now be compared to experimental [65,102] vacuum data for the K-edge (8.9 keV) TEY attenuation in Cu (fig. 3.35). The calculation was carried out including the Cu KLL (E_0 = 7000 eV, R_B = 2810 Å) and Cu LMM (E_0 = 920 eV, R_B = 128 Å) emission. Since the photon flux I_0 has not been reported for the experimental data [65,102] only a normalised edge step current $i(d)/i(0.5\ R_B)$ was evaluated [7]. Applying the 63.2% threshold predicts a probing depth of 380 Å, a value which is significantly lower than the probing depth obtained with an exponential fit (λ = 550 Å, also in fig. 3.35) to the dataset of Ebel *et al.* [65]. Note, however, that the results of Martens *et al.* [102] suggest stronger attenuation of the TEY at higher film thicknesses. The

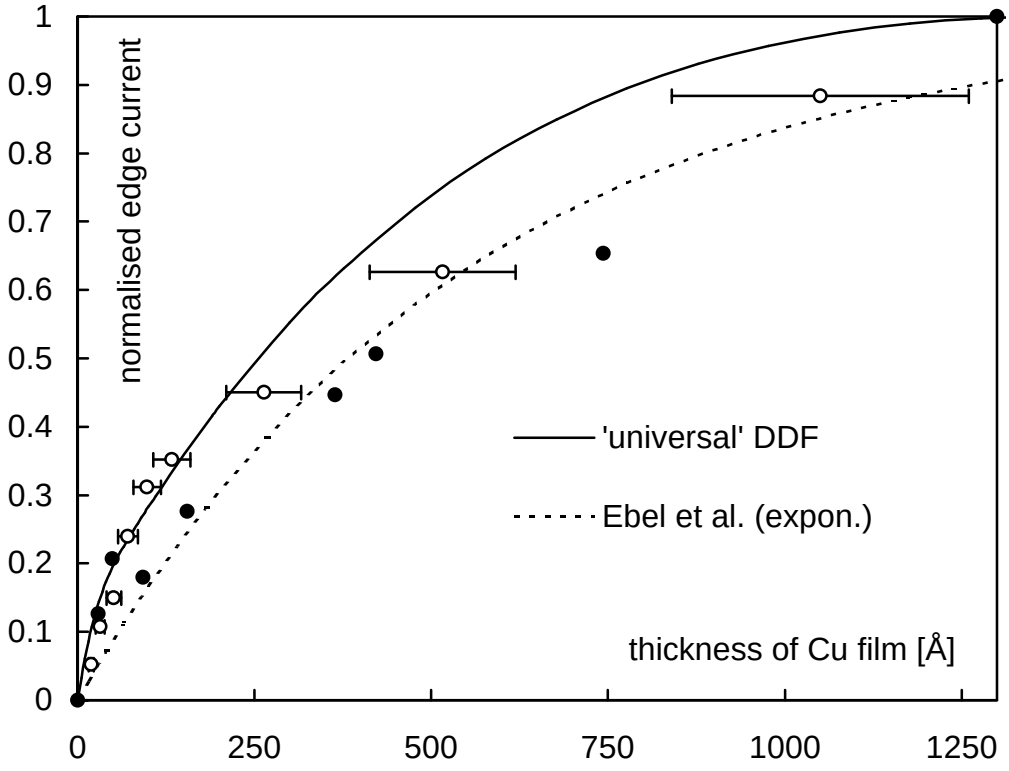

Figure 3.35. Experimental and measured Cu K-edge TEY signals from Cu films of varying thickness. Filled circles: data of Ebel *et al.* [65]; open circles: data of Martens *et al.* [102]; dashed line: exponential fit derived by Ebel *et al.* [65]; full line: result calculated with the Auger yield model based on the 'universal DDF'.

origin of the discrepancy between the experimental datasets is difficult to judge because few preparation and experimental details were given in the original work of Ebel *et al*. [65]. Nevertheless, the exponential fit reproduces both experimental datasets at higher film thicknesses (> 300 Å) better than the calculated Auger yield attenuation function, which clearly overestimates the TEY attenuation in this region. This result is certainly not unexpected because the calculation has neglected several factors which increase the signal of TEY contributions from deeper sample regions. These include straggling [73,82], oxidation, roughness and porosity of the Cu films as well as TEY contributions excited by self-absorbed fluorescent photons. Furthermore, a KLL induced secondary electron yield contribution is expected which should become more pronounced with increasing film thickness because of the larger numbers of heavily scattered KLL Auger electrons which arrive in the near-surface region. These electrons have relatively low energies and therefore shorter IMFPs, resulting in a higher probability for the excitation of secondary electrons. It is interesting that use of the 'universal' DDF affords very good agreement with experiment for film thicknesses below 200 Å where the influence of straggling and KLL induced secondary electrons must be weak (figure 3.35). Corrections to the calculated attenuation function in this region are mainly expected due to the LMM induced secondary electron yield and uncertainties in the LMM Bethe range (see section 3.7).

It has been verified that probing depth calculations based on the 'universal' DDF achieve similar agreement with other relevant data reported in the literature (see previous sections and [7,65,102]. As in section 3.9, these include attenuation data [9] for the O K-edge (0.5 keV) of Ta_2O_5, but exclude data for the Ni LMM (0.85 keV) attenuation in rare earth overlayers [9,10], indicating that the electron range in rare earths might be substantially shorter than predicted by the CSD approach. Future work should readdress the TEY signal attenuation especially at sub-keV absorption edges by using more advanced simulation algorithms based on exact scattering cross sections and improved stopping power calculations. Furthermore, the rôles of secondary electron production, straggling and self-absorbed fluorescence remain to be investigated. It is also desirable that the experimental database for TEY attenuation will be broadened, as currently available information is still very limited. More data are required to determine the limits of the present approach.

The main value of the 'universal' DDF is that it provides a simple, versatile method for semiquantitative predictions of the depth information in TEY data. It should be applicable to many materials (including compounds [96]). It avoids the arbitrariness of empirical extrapolations [65] and does not require the *a priori* knowledge of

several material-specific input parameters, as is the case for the often cited secondary yield model of Erbil *et al*. [7] The discussion of the results has shown that probing depth predictions based on the 'universal' Auger electron DDF should be regarded as lower limits to the true figures, especially for low-Z materials and thick samples. The method should be most reliable for gas-flow TEY data because the contributions of the secondary yield and low-energy Auger electrons are negligible in this detection mode.

3.11. Summary

For the first time Monte-Carlo algorithms have been employed to predict the attenuation characteristics of TEY XAS experiments. For a wide range of materials and absorption edge energies, it has been shown that the description of the TEY signal in terms of the Auger electron yield reproduces the depth information contained in the vacuum and gas-flow signals quite accurately. The comparison of calculated results with experimental TEY data has provided evidence that the calculation of the secondary electron contribution to the TEY is not crucial for achieving semiquantitative agreement with experiment. This considerable simplification allows simulation algorithms fast enough to be executed on small computers. Improvements to the presented algorithm are certainly possible. Future work should investigate the influence of secondary electron production and readdress the TEY signal attenuation at sub-keV absorption edges. Especially for the latter work it will be necessary to examine the CSD approximation and additivity rules for electron scattering properties of compounds. Both approaches might have to be replaced by more advanced calculation methods. Despite these current shortcomings, the quick Monte-Carlo approach presented here is clearly a rewarding method for the interpretation of the depth information contained in TEY data from any given sample specimen.

3.12. References

[1] R.R. Schaefer, J. Appl. Phys. 44 (1973) 152.

[2] W. Gudat, C. Kunz, Phys. Stat. Solidi 52 (1972) 433.

[3] W. Gudat, C. Kunz, Phys. Rev. Lett. 29 (1972) 169.

[4] B.L. Henke, Phys. Rev. A 6 (1972) 94.

[5] J. Stöhr, C. Noguera, T. Kendelewicz, Phys. Rev. B 30 (1984) 5571.

[6] J. Stöhr, *NEXAFS Spectroscopy (Springer Series in Surface Sciences 25)* (Springer, Berlin, Heidelberg, 1992).

[7] A. Erbil, C.S. Cargill III, R. Frahm, R.F. Boehme, Phys. Rev. B 37 (1988) 2450.

[8] A. Krol, C.J. Sher, Y.H. Kao, Phys. Rev. B 42 (1990) 3829.

[9] M. Abbate, J.B. Goedkopp, F.M.F. de Groot, J.C. Fuggle, S. Hofmann, H. Petersen, M. Sacchi, Surf. Interface Anal. 18 (1992) 65.

[10] J. Vogel, M. Sacchi, J. Electron Spectrosc. Relat. Phenom. 67 (1994) 181.

[11] S.L.M. Schroeder, G.D. Moggridge, R.M. Ormerod, T. Rayment, R.M. Lambert, Surf. Sci. Lett. 324 (1995) L371.

[12] M. Pollak, M. Gautier, N. Thromat, S. Gota, W.C. Mackrodt, V.R. Saunders, Nucl. Instrum. Methods B 97 (1995) 383.

[13] A. Caballero, J.P. Espinós, A. Fernández, D. Leinen, A.R. González-Elipe, Nucl. Instrum. Methods B 97 (1995) 397.

[14] A.M. Edwards, Y. Dao, R.J. Nemanich, D.E. Sayers, K.M. Kemner, J. Appl. Phys. 76 (1994) 4630.

[15] Y.U. Idzerda, W.T. Elam, B.T. Jonker, G.A. Prinz, Phys. Rev. Lett. 62 (1989) 2480.

[16] M.O. Krause, J. Phys. Chem. Ref. Data 8 (1979) 307.

[17] T. Mukoyama, Y. Ito, Nucl. Instrum. Methods B 87 (1994) 26.

[18] J.W. Cooper, J. Electron Spectrosc. Relat. Phenom. 67 (1994) 223.

[19] J.C. Woicik, P. Pianetta, S.L. Sorensen, B. Crasemann, Phys. Rev. B 39 (1989) 6048.

[20] S.B. Whitfield, G.B. Armen, R. Carr, J.C. Levin, B. Crasemann, Phys. Rev. A 37 (1988) 419.

[21] N. Mårtensson, R. Nyholm, B. Johansson, Phys. Rev. B 30 (1984) 2245.

[22] A.J. Dekker, Solid State Phys. 6 (1958) 251.

[23] H. Seiler, J. Appl. Phys. 54 (1983) R1.

[24] J. Schou, Scanning Microscopy 2 (1988) 607.

[25] S. Luo, D.C. Joy, Scanning Microscopy 4 (1990) 127.

[26] B.L. Henke, J. Liesegang, S.D. Smith, Phys. Rev. B 19 (1979) 3004.

[27] B.L. Henke, J.A. Smith, D.T. Attwood, J. Appl. Phys. 48 (1977) 1852.

[28] S. Hanany, P.S. Shaw, Y. Liu, A. Santangelo, P. Kaaret, R. Novick, Phys. Rev. B 48 (1993) 701.

[29] B.L. Henke, J.P. Knauer, K. Premaratne, J. Appl. Phys. 52 (1981) 1509.

[30] N.J. Shevchik, D.A. Fischer, Rev. Sci. Instrum. 50 (1979) 577.

[31] C.E. Bouldin, R.A. Forman, M.I. Bell, Phys. Rev. B 35 (1987) 1429.

[32] K. Kleinknecht, *Detectors for Particle Radiation* (Cambridge University Press, Cambridge, London, New York, 1986).

[33] B. Sitar, G.I. Merson, V.A. Chechin, Y.A. Budagov, *Ionization Measurements in High Energy Physics (Springer Tracts in Modern Physics, Vol.124)* (Springer-Verlag, Berlin, Heidelberg, New York, etc. 1993).

[34] *Handbook of Optical Constants of Solids* (Academic Press, Orlando, 1985).

[35] G.E. Jellison Jr. Thin Solid Films 234 (1993) 416.

[36] J.E. Castle, Nature Physical Science 234 (1971) 93.

[37] H. Uhlig, J. Pickett, J. MacNairn, Acta Met. 7 (1959) 111.

[38] J. Paidassi, *Métaux de la famille du fer,* in: L'oxydation des métaux. Tome II, Monographies, ed. by J. Bénard (Gauthier-Villars Éditeur, Paris, 1964) 117.

[39] W.A. Coghlan, R.E. Clausing, At. Data 5 (1973) 317.

[40] K. Siegbahn, C. Nordling, A. Fahlman, R. Nordberg, K. Hamrin, J. Hedman, G. Johansson, T. Bergmark, S.-E. Karlsson, I. Lindgren, B. Lindberg, *ESCA. Atomic, Molecular and Solid State Structure Studied by means of Electron Spectroscopy (Nova Acta Regiae Societatis Scientiarum Upsaliensis, Ser.IV Vol.20)* (Almqvist & Wiksells Boktryckeri Ab, Uppsala, 1967).

[41] W.T. Elam, J.P. Kirkland, R.A. Neiser, P.D. Wolf, Phys. Rev. B 38 (1988) 26.

[42] W.T. Elam, J.P. Kirkland, R.A. Neiser, P.D. Wolf, Physica B158 (1989) 295.

[43] A. Jablonski, Surf. Interface Anal. 20 (1993) 317.

[44] S. Tanuma, C.J. Powell, D.R. Penn, Surf. Interface Anal. 20 (1993) 77.

[45] C.J. Powell, Surf. Interface Anal. 7 (1985) 263.

[46] M.P. Seah, W.A. Dench, Surf. Interface Anal. 1 (1979) 2.

[47] H. Seiler, Z. f. angew. Physik 22 (1967) 249.

[48] D.C. Joy, J. Microsc. (Oxford) 147 (1987) 51.

[49] H. Salow, Phys. Z. 41 (1940) 434.

[50] H.A. Bethe, , *Phys. Rev.* 59 940.(1941) abstract

[51] D.C. Joy, *Monte Carlo Modeling for Electron Microscopy and Microanalysis (Oxford Series in Optical & Imaging Sciences. Vol. 9)* (Oxford University Press, New York, 1995).

[52] J. Schou, Scanning Microscopy 3 (1989) 429.

[53] S.C. Luo, D.C. Joy, Scanning Microscopy 2 (1988) 1901.

[54] L. Reimer, Scanning Electron Microsc. 11 (1979) 111.

[55] Z.-J. Ding, T. Nagatomi, R. Shimizu, K. Goto, Surf. Sci. 336 (1995) 397.

[56] K. Goto, N. Sakakibara, Y. Takeichi, Y. Numata, Y. Sakai, Surf. Interface Anal. 22 (1994) 75.

[57] Z.-J. Ding, R. Shimizu, K. Goto, J. Appl. Phys. 76 (1994) 1187.

[58] J.C. Greenwood, M. Prutton, R.H. Roberts, Z.X. Liu, Surf. Interface Anal. 20 (1993) 891.

[59] M.P. Seah, Surf. Interface Anal. 20 (1993) 865.

[60] M.P. Seah, Surf. Interface Anal. 20 (1993) 876.

[61] M.P. Seah, G.C. Smith, Surf. Interface Anal. 15 (1990) 751.

[62] A. Jablonski, C.J. Powell, Surf. Interface Anal. 20 (1993) 771.

[63] R.G. Jones, D.P. Woodruff, Surf. Sci. 114 (1982) 38.

[64] S.M. El-Mashri, R.G. Jones, A.J. Forty, Phil. Mag. A 48 (1983) 665.

[65] H. Ebel, M. Mantler, R. Svagera, R. Kaitna, Surf. Interface Anal. 22 (1994) 602.

[66] ASTM, Surf. Interface Anal. 17 (1991) 951.

[67] S.I. Salem, S.L. Panossian, S.O. Krause, At. Data Nucl. Data Tables 14 (1974) 91.

[68] N. Mårtensson, B. Johansson, Phys. Rev. B 28 (1983) 3733.

[69] V.L. Jacobs, J. Davis, B.F. Rozsnyai, J.W. Cooper, Phys. Rev. A 21 (1980) 1917.

[70] P. Weightman, P.T. Andrews, J. Phys. C 12 (1979) 943.

[71] R. Shimizu, Z.-J. Ding, Rep. Prog. Phys. 55 (1992) 487.

[72] D.C. Joy, Scanning Microscopy 5 (1991) 329.

[73] L. Reimer, R. Senkel, Optik 98 (1995) 85.

[74] R. Shimizu, Y. Kataoka, T. Matsukawa, T. Ikuda, K. Murata, H. Hashimoto, J. Phys. D: Appl. Phys. 8 (1975) 820.

[75] M. Kotera, K. Murata, K. Nagami, J. Appl. Phys. 52 (1981) 997.

[76] M. Kotera, K. Murata, K. Nagami, J. Appl. Phys. 52 (1981) 7403.

[77] L. Reimer, E.R. Krefting, *The Effect of Scattering Models on the Results of Monte Carlo Calculations,* in: Use of Monte Carlo Calculations in Electron Probe Microanalysis and Scanning Electron Microscopy (NBS Special Publications 460), ed. by K.F.J. Heinrich, D.E. Newbury and H. Yakowitz (National Bureau of Standards, Washington, D.C. 1976) 45.

[78] Z. Czyzewski, D.O. MacCallum, A. Romig, D.C. Joy, J. Appl. Phys. 68 (1990) 3066.

[79] A. Jablonski, S. Tougaard, Surf. Interface Anal. 22 (1994) 129.

[80] F. Salvat, R. Mayol, Comp. Phys. Comm. 74 (1993) 358.

[81] A. Jablonski, G. Gergely, Scanning 11 (1989) 29.

[82] R. Browning, T.Z. Li, B. Chui, J. Ye, R.F.W. Pease, Z. Czyzewski, D.C. Joy, J. Appl. Phys. 76 (1994) 2016.

[83] R. Gauvin, D. Drouin, Scanning 15 (1993) 140.

[84] D. Liljequist, F. Salvat, R. Mayol, J.D. Martinez, J. Appl. Phys. 65 (1989) 2431.

[85] R. Browning, Appl. Phys. Lett. 58 (1991) 2845.

[86] R. Browning, T. Eimori, E.P. Traut, B. Chui, R.F.W. Pease, J. Vac. Sci. Technol. B 9 (1991) 3578.

[87] D.C. Joy, S. Luo, Scanning 11 (1989) 176.

[88] M.J. Berger, S.M. Seltzer, *Tables of Energy-Losses and Ranges of Electrons and Positrons,* in: Studies in Penetration of Charged Particles in Matter (NAS-NRC Publication 1133), (National Academy of Sciences - National Research Council, Washington, D.C. 1964) 205.

[89] M.J. Berger, S.M. Seltzer, *NBS Internal Report 82-2550-A. Stopping Powers and Ranges of Electrons and Positrons (2nd Ed.)* (National Bureau of Standards, Washington, DC, 1983).

[90] R.F. Egerton, *Electron Energy-Loss Spectroscopy in the Electron Microscope* (Plenum Press, New York, London, 1986).

[91] G. Love, M.G.C. Cox, V.D. Scott, J. Phys. D: Appl. Phys. 10 (1977) 7.

[92] T.S. Rao-Sahib, D.B. Wittry, J. Appl. Phys. 45 (1974) 5060.

[93] W.H. Bragg, R. Kleeman, Phil. Mag. 10 (1905) 318.

[94] C. Tschalär, H. Bichsel, Phys. Rev. 175 (1968) 476.

[95] U. Fano, Annu. Rev. Nucl. Sci. 13 (1963) 1.

[96] R. Herrmann, L. Reimer, Scanning 6 (1984) 20.

[97] L.E. Porter, Nucl. Instrum. Methods B 95 (1995) 285.

[98] Z.-J. Ding, R. Shimizu, Surf. Interface Anal. 23 (1995) 351.

[99] R.L. Myklebust, D.E. Newbury, H. Yakowitz, *NBS Monte Carlo Electron Trajectory Calculation Program,* in: Use of Monte Carlo Calculations in Electron Probe Microanalysis and Scanning Electron Microscopy (NBS Special Publication 460), ed. by K.F.J. Heinrich, D.E. Newbury and H. Yakowitz (National bureau of Standards, Washington, D.C. 1976) 105.

[100] G. Tourillon, E. Dartyge, A. Fontaine, M. Lemmonnier, F. Bartol, Phys. Letters A 121 (1987) 251.

[101] T. Girardeau, J. Mimault, M. Jaouen, P. Chartier, G. Tourillon, Phys. Rev. B 46 (1992) 7144.

[102] G. Martens, P. Rabe, G. Tolkiehn, A. Werner, Phys. Stat. Sol. A 55 (1979) 105.

[103] S. Tanuma, C.J. Powell, D.R. Penn, Surf. Interface Anal. 17 (1991) 911.

[104] A.P. Walker, R.M. Lambert, J. Phys. Chem. 96 (1992) 2265.

[105] R.M. Nix, R.W. Judd, R.M. Lambert, Surf. Sci. Lett. 215 (1989)

[106] D.M. Jaffey, Ph. D. -Thesis,University of Cambridge (1987)

[107] R.M. Nix, Ph. D. -Thesis,University of Cambridge (1987)

[108] R.M. Nix, R.M. Lambert, Surf. Sci. 186 (1987) 163.

[109] R.G. Jones, personal communication (1995)

[110] D. Norman, D.P. Woodruff, Surf. Sci. 75 (1978) 179.

[111] S. Tanuma, C.J. Powell, D.R. Penn, Surf. Interface Anal. 17 (1991) 927.

[112] S. Tougaard, Surf. Interface Anal. 11 (1988) 453.

[113] D.I. Thwaites, Nucl. Instrum. Methods B 69 (1992) 53.

[114] J. Löffler, M. Weissmüller, Phys. Rev. B 52 (1995) 7076.

[115] W.W. Smeltzer, D.J. Young, Progress in Solid State Chemistry 10 (1975) 17.

[116] O. Kubaschewski, B.E. Hopkins, *Oxidation of Metals and Alloys* (Butterworths, London, 1967).

[117] D. Liljequist, T. Ekdahl, U. Bäverstam, Nucl. Instrum. Methods 155 (1978) 529.